Bitumen Liberation Dynamics

by

Bauyrzhan Kerimkulovich PRIMKULOV

A thesis submitted in partial fulfillment of the requirements for the degree of

Master of Science

in

Chemical Engineering

Department of Chemical and Materials Engineering

University of Alberta

Abstract

The minable oil sands extraction process can be understood on a scale of a single oil sand grain. When the oil sand ore is mixed with warm water, each sand granule is initially covered with bitumen film which ruptures under the composite effect of shear and interfacial forces, while water spontaneously displaces bitumen until the droplets reach their equilibrium shape. The dynamics of this process is known to be sensitive to the temperature of the slurry and chemical additives. Therefore, understanding the governing mechanisms of dynamic wetting is crucial for finding optimal operating conditions for oil sand extraction process. This work utilized modified micro-pipette technique to investigate bitumen droplet recession on micro-spherical glass surface. The dynamic shape evolution of the bitumen droplet was modeled with hydrodynamic, molecular-kinetic, and combined wetting models. The effect of water chemistry, temperature, and diluent addition to bitumen was evaluated in the light of dynamic wetting models. It was found that the work of adhesion along with the ratio of bitumen-water interfacial tension to viscosity were critical rate controlling parameters for bitumen displacement. The combined molecular-hydrodynamic model was further extended to wetting in capillary tubes, revealing possible enhancements to in-situ oil recovery from porous media.

Preface

Some of the research conducted for this thesis forms part of a research collaboration, led by Professor Zhenghe Xu and Dr. Feng Lin. Utilizing a modified micro-pipette technique along with the application of dynamic wetting theories to the system of this study were developed by Dr. Lin, who also provided the interfacial tension data referred to in chapter 2. I was responsible for conducting bitumen droplet recession experiments and performing the data analysis. The concluding analysis in chapters 4 and 5 are my original work, as well as the literature review in chapters 1 and 3.

Parts of the literature review and data in Chapter 4 of this thesis are being considered for publication. I was responsible for the data collection and analysis as well as the manuscript composition. Professor Zhenghe Xu and Dr. Feng Lin were the supervisory authors and were involved in revision of the manuscript.

"I was in the cafeteria and some guy, fooling around, throws a plate in the air. As the plate went up in the air I saw it wobble, and I noticed the red medallion of Cornell on the plate going around. It was pretty obvious to me that the medallion went around faster than the wobbling.

I went on to work out equations of wobbles. Then I thought about how electron orbits start to move in relativity. Then theres the Dirac Equation in electrodynamics. And then quantum electrodynamics. And before I knew it (it was a very short time) I was playing working, really with the same old problem that I loved so much, that I had stopped working on when I went to Los Alamos: my thesis-type problems; all those old-fashioned, wonderful things.

It was effortless. It was easy to play with these things. It was like uncorking a bottle: Everything flowed out effortlessly. I almost tried to resist it! There was no importance to what I was doing, but ultimately there was. The diagrams and the whole business that I got the Nobel Prize for came from that piddling around with the wobbling plate."

Richard P. Feynman

Acknowledgements

Contents

List of Tables

List of Figures

Symbols

A	bitumen-sand interfacial area	m^2
Ca	capillary number	
$\dot{E}_l$	wetting line friction loss per unit length of contact line	$J \cdot s^{-1} \cdot m^{-1}$
$\dot{E}_w$	viscous dissipation in liquid bulk per unit length of contact line	$J \cdot s^{-1} \cdot m^{-1}$
G	Gibbs free energy	J
h	Planck's constant	$m^2 \cdot kg \cdot s^{-1}$
k_B	Boltzmann constant	$m^2 \cdot kg \cdot s^{-2} \cdot K^{-1}$
K_b	frequency of bitumen molecule displacing water from glass surface per unit time per unit length of wetting line	s^{-1}
K_w	frequency of water molecule displacing bitumen from glass surface per unit time per unit length of wetting line	s^{-1}
$L(t)$	instantaneous *curved* length of wetted region (see Figure 3.1)	m
r_o	instantaneous radius of bitumen droplet	m
r_m	radius of micro-spherical glass substrate	m
T	temperature	K
U	three-phase contact line displacement rate	$m \cdot s^{-1}$
W_a	work of adhesion	$J \cdot m^{-2}$
γ_{SW}	sand-water interfacial tension	$J \cdot m^{-2}$
γ_{BS}	bitumen-sand interfacial tension	$J \cdot m^{-2}$
γ_{BW}	bitumen-water interfacial tension	$J \cdot m^{-2}$

θ_S	static contact angle, measured from water phase	rad
θ	dynamic contact angle, measured from water phase	rad
μ_b	viscosity of bitumen	$Pa \cdot s$
μ_w	viscosity of water	$Pa \cdot s$

Chapter 1

Introduction

1.1   Oil Sands Extraction Process

First records of Athabasca Oil Sands date back to 1719. At that time, bitumen was used by aboriginal people to waterproof canoes and ward off mosquitoes. Eventually, the word about the Athabasca oil sands spread out in North America, and first attempts of trade were made. Explorers realized fuel supply potential of Athabasca region and started developing bitumen recovery methods. This led to Sidney Ells' discovery of hot water-based extraction process in 1915, which prompted first commercial developments of bitumen reserves [1].

Viscous nature of bitumen crude made it impossible to extract it with conventional production wells. Bitumen did not flow under standard conditions, and its viscosity was well above $500 Pa * s$ at room temperature [2]. Hence, the most viable option was to develop oil sands reserves with open pit mining, which is a prevailing method in Athabasca operations even today.

Clark and Pasternack [3] hot water based process lies at the heart of modern mineable oil sands extraction. Freshly mined ores are crushed and mixed with hot water and chemicals to prepare a slurry at $50°C$. The mixture is then pumped through hydro-transport pipelines into separation vessels, where small air bubbles

(A) oil sand grain

(B) film rupture

(C) towards libera-
tion

(D) aeration
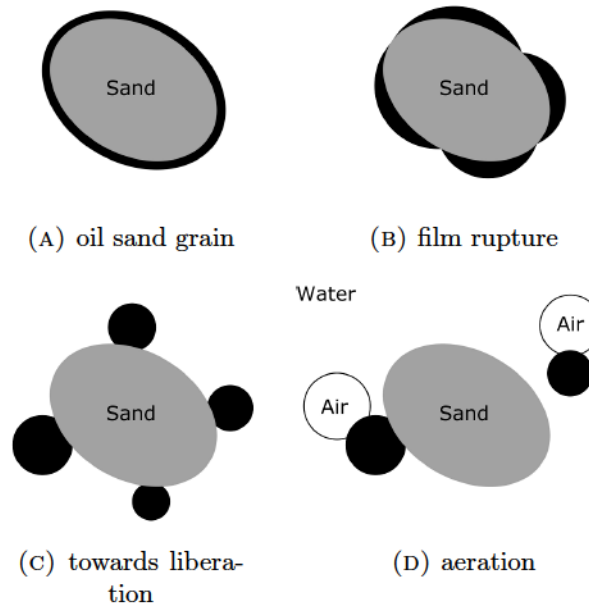
FIGURE 1.1: Schematic demonstration of bitumen extraction steps on a single
oil sand grain

are introduced to the system. Bitumen droplets attach to air bubbles and float to
the top, forming a bitumen-rich phase.

Bitumen extraction process involves, but not necessarily limited to, the three
important fundamental steps: bitumen film rupture, liberation, and aeration. I
discuss each of these steps in a few sections below.

1.1.1 Film Thinning and Rupture

When oil sands ore is mixed with hot water and pumped through a hydro-transport
pipeline, high temperature and shear stress ablate larger ore lumps into separate
oil sand grains (Figure 1.1a). Each sand grain is initially covered with a bitumen
layer, which thins under composite effect of process water chemistry and operating
conditions.

According to Vrij [4], early stages of film thinning are normally governed by gravity
and hydrodynamic effects. Other forces become increasingly important, as the film
thickness is reduced to about $100nm$. Van der Waals attractive force assists film

drainage, while double layer (or other forces) resists it. At this stage, films are very stable and difficult to break.

Further thinning prompts liquid film to enter a metastable state, where attractive and repulsive forces are balanced. Spontaneous rupturing of metastable films still requires high activation energy; hence mostly film rupture occurs due to thermal shock, vibrations, and contaminants [4].

If the film enters unstable state, characterized by critical thickness; it ruptures spontaneously due to small surface perturbations [5]. Ruckenstein and Jain [6] analyzed spontaneous rupture of thin films, and highlighted stabilizing effect of surfactants. Surface active impurities dampen disturbances that occur at liquid interface, increasing rupture time by several orders of magnitude.

1.1.2 Liberation

Once bitumen film ruptures, a three-phase contact line is formed on sand grain surface (Figure 1.1b). At the wetting line, water spontaneously displaces bitumen from sand grain surface until bitumen phase forms droplets of optimal shape (Figure 1.1c).

The whole process can be qualitatively analyzed with the approach of Masliyah et al. [2], assuming that changes in bitumen-water interfacial area are negligible. Then, change in Gibbs free energy of bitumen recession can be written as

$$\Delta G = \gamma_{SW} \Delta A - \gamma_{BS} \Delta A. \tag{1.1}$$

By combining relation (1.1) with Young's equation, we can obtain simplified governing equation for bitumen recession

$$\frac{\Delta G}{\Delta A} = -\gamma_{BW} \, cos\theta_S, \tag{1.2}$$

where static contact angle θ_S is measured from water phase.

As long as static contact angle of bitumen phase is smaller than 90°, change in Gibbs free energy is negative, and bitumen recession is spontaneous. Generally, smaller values of static contact angle make expression (1.2) more negative, which makes bitumen recession faster. This analysis confirms the intuitive notion that oil is displaced by water faster from hydrophilic substrates.

1.1.3   Aeration

When bitumen droplets obtain their static shape, one would want to detach bitumen phase from sand surface. In idealized case of this separation, bitumen-sand contact area is replaced by equivalently large areas of bitumen-water and sand-water interfaces. Associated change in Gibbs free energy is as follows:

$$\Delta G = \gamma_{SW}\Delta A + \gamma_{BW}\Delta A - \gamma_{BS}\Delta A. \tag{1.3}$$

Once again, we incorporate Young's equation to derive governing relation for bitumen detachment from a substrate as follows:

$$\frac{\Delta G}{\Delta A} = \gamma_{BW}(1 - cos\theta_S). \tag{1.4}$$

Since $(1 - cos\theta_S)$ is never negative, equation (1.4) suggests that bitumen does not separate spontaneously from sand surface. Additional work has to be done to facilitate the detachment. In industrial oil sands extraction, this is done by introducing fluid drag in hydro-transport pipeline and increasing droplet buoyancy by adding air bubbles to oil sand slurry.

1.2   Thesis Objectives

The main focus of this thesis is on bitumen liberation dynamics. We examine governing mechanisms of liquid-liquid displacement from solid surfaces, exploring major driving forces and restraining factors. Major parameters defining the

displacement rate are explored along with implications for oil sands extraction.

1.3   Background

1.3.1   Experimental Studies of Bitumen Liberation

A number of studies on bitumen recession dynamics were performed in the past. A general notion was developed that chemical additives, pH, temperature, and shear rate play important roles in defining rate of bitumen liberation [2].

Walker [7] studied bitumen displacement from microscope slides in flowing water, under controlled conditions. Rates of bitumen displacement were estimated from darkness of bitumen-coated glass. When flowing water temperature was increased from $35°C$ to $60°C$, bitumen liberation rates increased by one order of magnitude. This was mostly attributed to lower viscosity of heated bitumen phase. Additionally, Walker [7] observed that addition of Ca^{2+} ions was detrimental for bitumen liberation.

Basu et al. [8] investigated bitumen liberation at a smaller scale. Clean microscope slides were coated with circular layer of bitumen of $9mm$ in diameter and $0.7mm$ in thickness. Then, the set up was placed into a water bath of controlled pH and temperature. Spontaneous bitumen droplet recession was tracked with a high speed camera, and temporal evolution of contact angle was obtained from resulting images. Basu et al. [8] gave a quantitative description to bitumen droplet recession, and was able to link positive effect of high solution temperature (and low viscosity) with lower hydrodynamic losses in bitumen phase. At the same time, the effect of solid-liquid interaction was only discussed qualitatively. Higher values of pH resulted in lower static contact angles, which meant that pH was capable of altering interfacial properties of the system.

Bitumen displacement from silica surfaces can be viewed as part of a larger pool of studies on wetting dynamics. Investigation of three phase contact line motion was

initially fueled by interest in surface coating, detergency, painting, and lubrication applications. Significant advances were made in understanding physics of wetting lines in recent years. Careful consideration of major theoretical developments in this field, can lead to better understanding of bitumen liberation physics.

1.3.2 Wetting Dynamics

Majority of the previous work in wetting dynamics focused on liquid/gas/solid systems. A typical example would be spreading of a small liquid droplet on smooth, homogeneous, flat surface in air. To quantify the process most investigators took either molecular-kinetic or hydrodynamic approaches, which differ mostly in consideration of dominant energy dissipation mechanisms. Both models are widely implemented in numerous liquid-gas experiments, and often both can be fitted well to the same experimental data. There are several thorough reviews [9–11] available on liquid-gas displacement from solid surfaces. On the other hand, liquid-liquid displacement on a solid surface has been investigated sparsely, and new insights were revealed only recently.

Some of the first liquid-liquid displacement experiments were analyzed using hydrodynamic approach. Foister [12] investigated spontaneous displacement of one liquid by another from smooth solid surfaces. He used immiscible liquids of wide viscosity range and observed that viscosity ratio can have a significant effect on the rate of displacement. Foister [12] tied his experimental observations with hydrodynamic theory of Cox [13], where liquid viscosity ratio plays a critical role. Essentially hydrodynamic approach assumes that three-phase contact line is driven by capillary forces while excess energy is lost through viscous dissipation in either liquid. However, Fermigier and Jenffer [14] pointed out that purely hydrodynamic model systematically underestimates dynamic contact angles when carefully compared with experimental observations. In fact, Sheng and Zhou [15] suggested that another dissipation mechanism might play an important role, especially below certain capillary number range, where capillary number is defined as $Ca = \frac{\mu U}{\gamma}$.

At low capillary numbers viscous dissipation in liquid bulk becomes negligible and contact line displacement rate is controlled by adsorption/desorption processes described in molecular-kinetic theory of Blake and Haynes [16]. This approach suggests that majority of energy dissipation takes place within immediate vicinity of three phase contact line, and displacement rate depends on the nature of liquid-solid interactions. Ramiasa et al. [17] investigated slow displacement of water by dodecane droplets from thiol-coated gold surfaces. Immiscible liquid phases were kept constant, while substrate wettability was altered by applying varying degrees of thiol coating. Ramiasa et al. [17] was able to demonstrate experimentally that whenever molecular-kinetic approach was applicable, wetting line energy dissipation changed exponentially with work of adhesion.

Fetzer et al. [18] suggested that it is possible to decide based on capillary number range whether molecular-kinetic or hydrodynamic mechanisms control the rate of wetting line motion. They established that molecular-kinetic approach describes liquid-liquid displacement from solid surfaces very well, as long as associated capillary numbers are below $2*10^{-4}$. In the range of capillary numbers above $2*10^{-4}$, Fetzer et al. [18] recommended hydrodynamic models although they still produced unrealistic fitting parameters. Authors explained the discrepancy by possible inertial deterioration of contact line motion at high displacement rates. Later, Lin et al. [19] investigated a series of dynamic wetting experiments at a microscopic scale, where inertial effects could be safely neglected. They found that in certain cases both molecular-kinetic and hydrodynamics based models produce good fit to experimental data. This finding suggests that there might be a range of experimental conditions where both adsorption/desorption mechanisms and hydrodynamic dissipation in liquid bulk could have comparable control over liquid-liquid displacement rates.

1.4   Thesis Contributions

In this thesis, we examined spontaneous displacement of bitumen droplet by water from micro-spherical glass surfaces using a modified micro-pipette technique. We tested applicability of hydrodynamic and molecular-kinetic models, and found capillary number ranges where combined molecular-hydrodynamic model should be considered. Moreover, we investigated how aqueous solution pH, electrolyte concentration, temperature, substrate wettability, and diluent addition impact bitumen displacement dynamics.

1.5   Thesis Outline

Chapter 1 gives a brief introduction to bitumen extraction process and provides the literature review for previous bitumen liberation studies as well as the current state of knowledge in the field of dynamic wetting.

Chapter 2 describes the procedures for droplet relaxation experiments used in this study. This chapter includes details on substrate preparation, coating, experimental conditions, and material characterization.

Chapter 3 is concerned with building quantitative models of bitumen droplet recession from micro-spherical substrate. Two dynamic wetting models based on hydrodynamic and molecular-kinetic theories, along with more recent combined approach are derived for the current spherical system in detail.

Chapter 4 discusses the experimental and theoretical modelling results. The three models developed for our experimental geometry as described in chapter 3 are applied to evaluating and understanding experimentally-observed temporal evolution of apparent contact angles. Effect of solid-liquid interactions, substrate wettability, pH, temperature, concentration of aqueous electrolytes and addition of diluent to bitumen on wetting dynamics is discussed along with their implications for industrial applications.

Chapter 5 extends our view of dynamic wetting to the flow in porous media. Some of the most common in-situ recovery techniques such as SAGD and water flooding are discussed in terms dynamic wetting.

Chapter 6 summarizes major findings of this work. The details of our newly-developed automated angle acquisition technique are given in Appendix A.

Chapter 2

Materials and Methods

2.1 Droplet Relaxation Experiment

Bitumen droplet relaxation on spherical glass substrate was investigated utilizing a modified micro-pipette technique [19]. Micro-pipette technique was initially introduced by Yeung et al. [20, 21, 22, 23] into the research of oil sands and emulsions. This technique was further modified to suit the requirements of the current study. Here, the procedure of so-called droplet relaxation experiment is described. In this study micron scale, ball shaped, glass tips were coated with bitumen in air. Then the sample was placed into aqueous solution, where bitumen droplet spontaneously receded from the substrate (Figure 2.1). The whole process was recorded with high-speed camera under optical microscope (Zeiss Axiovert 200). Resulting images were analyzed with automated angle acquisition method described in detail in appendix A.

t=6sec   t=60sec   t=3000sec   20μm ⊢───┤
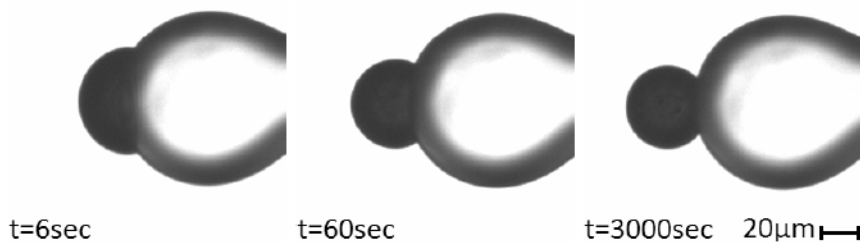
FIGURE 2.1: Typical bitumen micro-droplet relaxation images

FIGURE 2.2: Substrate preparation images: a) a sharp micro-pipette tip obtained after stretching in hot-wire puller; b) the substrate is further melted until a sphere of desired size is acquired

2.1.1 Preparation and Treatment of Solid Substrate

Substrates were prepared from clean glass capillary tubes (Drummond Scientific $30\mu L$ Microcaps). Each tube was 78mm in length and 1mm in diameter. First, glass pipettes were axially stretched using hot-wire puller (David Kopf Inst. 730) until separated into two. By doing so, we produced close-ended pipettes with needle-like tips as shown in Figure 2.2a. Resulting tapered hollow tubes were further melted by a hot platinum wire to form spherically shaped tips as shown in Figure 2.2b. The size of the micro-spheres was carefully controlled to $35\mu m$ in radius with less than 5% deviation.

High temperature treatment of the glass capillaries served several purposes. Firstly, by bringing micro-pipette tips above the glass transition temperature we were able to generate very smooth and homogeneous substrate surfaces. Secondly, we could safely assume that all of the organic impurities were removed during this process, since glass transition point was above $550°C$. Finally, by approaching the glass transition point, we most likely removed hydroxyl group from the glass surface. The freshly fabricated micro-spherical tips were shown to be less hydrophilic in nature.

The substrate wettability was adjusted by controlled hydrolysis. The freshly prepared micro-spherical glass tips were immersed in the baseline aqueous solution (section 2.1.3) for a period of time prior to bitumen coating and displacement experiments. The longer the glass was exposed to water, the higher was its affinity to aqueous phase and hence the higher the water-wettability.

2.1.2 Bitumen Phase

Coker-feed bitumen used in this study was provided by Syncrude Canada. Bitumen is a highly viscous, complex mixture of heavy organic components, with significant presence of naphthenes and aromatics [2]. On an elemental level, bitumen is mostly composed of carbon (83.1%), hydrogen (10.3%), nitrogen (0.4%), oxygen (1.1%), sulfur (4.6%), and some metals [24]. Relatively low hydrogen to carbon ratio is normally explained by depositional history of Athabasca bitumen. Original oil accumulated in a formation with high bacterial activity, and hydrogen-rich light hydrocarbon components were consumed as a food source by the bacteria. Leftover organics formed resultant Athabasca bitumen.

2.1.3 Aqueous Phase

Aqueous solutions were prepared from deionized water, to which certain amounts of salts were added to mimic industrial process water. A baseline solution contained 100 ppm of $NaHCO_3$ and 500 ppm of $NaCl$, and its pH was controlled at 8 by addition of $NaOH$. This solution was further modified to study the effect of Ca^{2+}, Na^+ and pH on bitumen displacement dynamics.

2.1.4 Experimental Specifications

The effect of solution pH, $NaCl$ and $CaCl_2$ concentrations on wetting dynamics was explored on freshly fabricated micro-spherical tips. Aqueous phase was prepared by adjusting the baseline aqueous solution (section 2.1.3), while bitumen phase and substrate were kept constant. This series of experiments were conducted at room temperature.

The effect of temperature was investigated on a baseline solution with pH value of 8. Each of the displacement tests was conducted on freshly prepared micro-spherical substrates. Before the tests, aqueous solution was pre-heated to a desired temperature. It is important to note that, when solution temperature was elevated
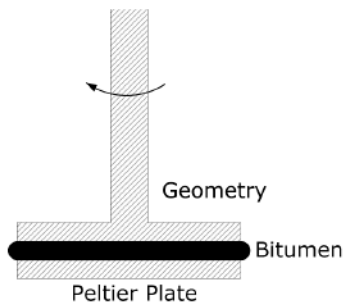
FIGURE 2.3: Schematic diagram of rotational rheometer

to 50°C and higher, the bitumen droplet liberation took only a few seconds. Thus, we can assume that the temperature was constant throughout the displacement, even without an external system for temperature control.

2.2 Bitumen Viscosity Measurement

Bitumen behaves as a Newtonian fluid [2], and its viscosity is independent of induced shear rate. However, great care should be taken when conducting bitumen viscosity measurements. During the measurements, bitumen temperature might increase due to viscous dissipation, which makes the liquid exponentially less resistant to flow. Thus, one should carefully control bitumen temperature when applying shear to it.

TA Instuments ARES-2G rotational rheometer was used to measure bitumen viscosity at controlled temperatures. In principle, the rheometer consists of a Peltier plate and a spindle, to which different geometries are attached (Figure 2.3). The base plate has a mounted temperature control system, which is cooled by circulating water bath and heated electrically.

Bitumen samples were placed between the Peltier base and 20-mm-diameter parallel plate geometry. The sample volume was carefully controlled at about 0.06 mL. This was important since overfilling or underfilling of the sample holder could result in biased viscosity readings. Viscosity data was obtained by increasing the shear rate from $0.01s^{-1}$ to $2.00s^{-1}$, while temperature was controlled at 25°C,

50°C, or 70°C. Figure 2.4 shows reliable viscosity measurements with minimal viscous heating effects. Temperature had a significant impact on bitumen viscosity - as the bitumen temperature was increased from 25°C to 70°C, the viscosity values dropped from $1041 Pa \cdot s$ to $8.8 Pa \cdot s$.

2.3 Interfacial Tension Measurement

Measuring bitumen-water interfacial tension at room temperature is a challenging task. Bitumen density is almost identical to density of water. As a result, any of the techniques that rely on density differentials (pendant drop, sessile drop, spinning drop) would not be effective. Moreover, matched density of bitumen and water phases makes it very difficult to obtain a flat liquid-liquid interface. Hence, force-based tension experiments (Wilhelmy plate, Du Noüy ring) would have a significant bias too.

In this study bitumen-water interfacial tension values were obtained using micro-emulsion drop-shape recovery technique introduced by Moran et al. [25]. Here, micron-scale bitumen droplet was axially stretched with suction pipettes. Then, the droplet was released on one end, and allowed to recover to an optimal shape (Figure 2.5). The droplet motion was driven by bitumen-water interfacial tension
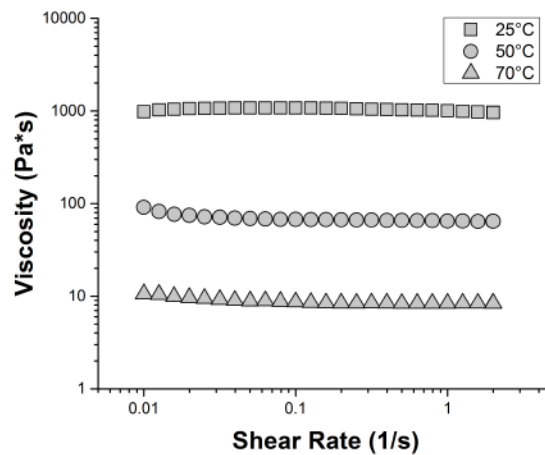
FIGURE 2.4: Bitumen viscosity measured at controlled temperatures
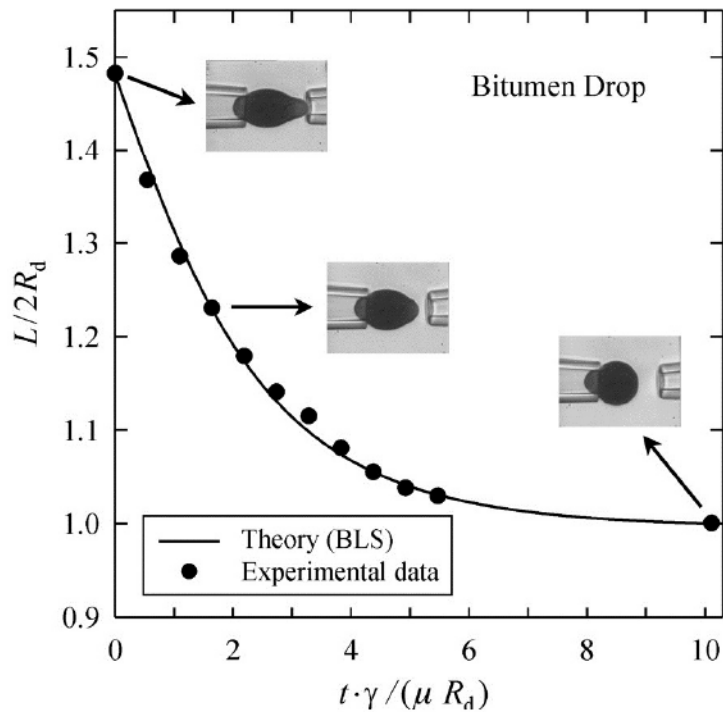
FIGURE 2.5: Figure from Moran et al. [25], showing typical bitumen drop shape recovery experiment, fitted with the boundary least squares approach. R_d is the radius of the drop in its spherical state. L is instantaneous axial length of the droplet. t, γ, μ are droplet relaxation time, interfacial tension, and bitumen viscosity.

TABLE 2.1: Results of oil-water interfacial tension measurements

Aqueous Solution	$NaCl$ (ppm)	$CaCl_2$ (ppm)	pH	γ (mJ/m^2)
baseline	500	0	8.0	13.92
Ca100	500	100	8.0	14.26
Ca200	500	200	8.0	15.24
Na1000	1000	0	8.0	10.01
Na2000	2000	0	8.0	9.78
pH10	500	0	10.0	7.94
pH11	500	0	11.0	4.89

and retarded by viscous resistance of bitumen phase. Hence, by fitting the *boundary least squares* solution of droplet relaxation [25], we could obtain the ratio of interfacial tension to viscosity $(\frac{\gamma_{BW}}{\mu})$. With a known value in viscosity of bitumen, bitumen-water interfacial tension could be obtained.

By adjusting the water chemistry including pH, sodium and calcium ion concentrations, bitumen-water interfacial tensions were altered, and the measured results

are shown in Table 2.1. Athabasca bitumen is known to contain natural surfactants, which have hydrophilic head groups and hydrophobic tails. Hence, when bitumen makes contact with water, surface-active components migrate from the bitumen bulk to bitumen-water interface [2]. Increasing the aqueous solution pH ionizes surfactant head groups, making them more soluble in water. *As a result, increasing pH facilitates the accumulation of natural surfactant molecules from the bulk bitumen onto the interface and their consequent migration into the aqueous phase* [2]. This observation explains the reduction of interfacial tension at higher pH values in Table 2.1. Addition of Calcium ions, on the other hand, increases the bitumen-water interfacial tension. Calcium ions are known to react with the natural surfactant head groups, forming calcium salts of very low water solubility [2]. This results in smaller concentrations of surfactants in aqueous phase, and thus accumulation of the surfactants at the bitumen-water interface also reduces. Finally, addition of Sodium ions to the aqueous solution causes relatively small reductions in bitumen-water interfacial tension (Table 2.1). It is possible that high electrolyte concentrations screen charged surfactant head groups, allowing additional surfactant adsorption to the interface.

Chapter 3

Theory of Dynamic Wetting

3.1   Geometric Relations

Let us consider a small bitumen droplet on smooth spherical glass surface (Figure 3.1). We limit our attention to micrometer-scale oil droplet surrounded by aqueous phase. In all of our experiments both Bond number (ratio of gravitational to capillary forces) and Weber number (ratio of inertial to capillary forces) were many orders of magnitude smaller than one, so gravitational and inertial effects can be safely neglected. Initially the system is at non-equilibrium state, and the droplet recedes spontaneously from the substrate to attain optimal energy state.

Considering that the motion is driven by capillary forces, we assume that bitumen phase maintains truncated spherical cap shape on the glass sphere for the duration
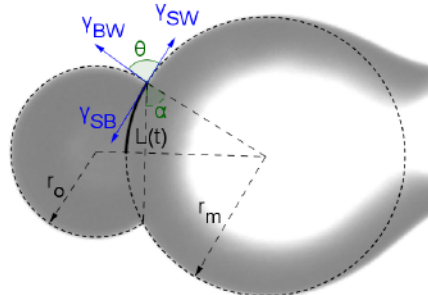
FIGURE 3.1: Schematic view of bitumen droplet on spherical glass surface

17

of relaxation. Then droplet volume can be expressed as

$$V = \frac{\pi}{3}r_o^3[2 + 3sin(\alpha + \theta) - sin^3(\alpha + \theta)] - \frac{\pi}{3}r_m^3[2 - 3sin(\alpha) + sin^3(\alpha)]. \quad (3.1)$$

Since bitumen is immiscible with water, the droplet volume should remains constant throughout the process, where angles θ and α change as a function of time. Therefore, by setting first derivative of the volume expression (3.1) equal to zero, we can obtain useful geometric relationship between the two angles

$$\frac{d\theta}{dt} = -\frac{sin\theta(2 - sin(\theta + \alpha))}{cos\alpha}\frac{d\alpha}{dt}. \quad (3.2)$$

Here angle α can be further linked to the size of bitumen-covered glass surface ($\frac{dL(t)}{dt} = -r_m\frac{d\alpha}{dt}$). Thus, the rate of the contact angle change can be related to the speed of the wetting line

$$\frac{d\theta}{dt} = \frac{sin\theta(2 - sin(\theta + \alpha))}{r_m\,cos\alpha}U, \quad (3.3)$$

where equation (3.7), (3.11), or (3.16) can be used for U, depending on whether hydrodynamic, molecular-kinetic, or combined approach is taken.

3.2 Hydrodynamic Model

Hydrodynamic consideration of slow wetting line motion typically involves solving creeping flow equation in the vicinity of the three phase contact line. Huh and Scriven [26] were among the first to take this approach when investigating flow near simple wetting line wedge. Taking a conventional no-slip boundary condition between the liquid and solid, they found that hydrodynamic solution results in unbounded stress at the wetting line [26]. This unbounded stress is a common problem to all hydrodynamic solutions of dynamic wetting, which is normally attributed to rheological anomalies and breakdown of continuum approximation at

the contact line. One way around this problem is to relax no-slip boundary condition in immediate neighborhood of wetting line, hence a typical hydrodynamic solution would include a phenomenological slip-length parameter L_m.

One of the most complete hydrodynamic solutions of liquid-liquid displacement at the solid surface was developed by Cox [13, 27]. He divided wetting line neighborhood into inner, intermediate, outer regions and used matched asymptotic expansions to link apparent contact angle with the wetting line velocity. The resulting solution, to the lowest order in capillary number, is as follows

$$U = \frac{\gamma_{BW}\left(g(\pi - \theta, \frac{\mu_w}{\mu_b}) - g(\pi - \theta_S, \frac{\mu_w}{\mu_b})\right)}{\mu_b \, ln(L/L_m)}, \tag{3.4}$$

where U is the wetting line velocity, θ is the dynamic contact angle, θ_S is the static contact angle, γ_{BW} and μ_b are bitumen-water interfacial tension and bitumen viscosity, L and L_m are macroscopic and microscopic length scales of the system. Function $g(\pi - \theta, \frac{\mu_w}{\mu_b})$ is defined as

$$g(\pi - \theta, \frac{\mu_w}{\mu_b}) = \int_0^{\pi-\theta} \frac{d\beta}{f(\beta, \frac{\mu_w}{\mu_b})} \tag{3.5}$$

and

$$f(\beta, \frac{\mu_w}{\mu_b}) = \frac{2sin\beta\left[(\frac{\mu_w}{\mu_b})^2\{\beta^2 - sin^2\beta\} + 2\frac{\mu_w}{\mu_b}\{\beta(\pi - \beta) + sin^2\beta\} + \{(\pi - \beta)^2 - sin^2\beta\}\right]}{\frac{\mu_w}{\mu_b}(\beta^2 - sin^2\beta)\{(\pi - \beta) + sin\beta cos\beta\} + \{(\pi - \beta)^2 - sin^2\beta\}(\beta - sin\beta cos\beta)} \tag{3.6}$$

We should note that in our system, bitumen viscosity is many orders of magnitude greater than viscosity of water. Thus, $\frac{\mu_w}{\mu_b}$ is negligibly small, and $f(\beta, \frac{\mu_w}{\mu_b})$ in equation 3.5 can be substituted with $\frac{2sin\beta}{\beta - sin\beta cos\beta}$. Furthermore, according to Voinov [28], $\int_0^{\pi-\theta} \frac{\beta - sin\beta cos\beta}{2sin\beta} d\beta$ can be approximated with $\frac{(\pi-\theta)^3}{9}$, as long as $(\pi - \theta)$ is smaller than 135°. Therefore, Cox [13] hydrodynamic solution takes its simplest form, resulting in the following governing equation

$$U = \frac{\gamma_{BW}\left((\pi - \theta)^3 - (\pi - \theta_S)^3\right)}{9\,\mu_b \, ln(L/L_m)}, \qquad for \; \theta > \pi/4, \tag{3.7}$$

Essentially, in hydrodynamic solution, surface tension along with the imbalance of dynamic and static contact angles drive the droplet towards optimal shape, while viscous dissipation in the bulk of the droplet retards the wetting line motion. It is important to note that microscopic length scale L_m is not known a priory, and it is often used as a fitting parameter to experimental observations. This slip length is expected to be no smaller than molecular length scale [10], and thus systems with smaller fitted values of L_m could be governed by other mechanisms.

3.3 Molecular-Kinetic Model

Molecular-kinetic approach [16] suggests that wetting rate can be controlled by adsorption-desorption processes at the wetting line. It assumes that solid surface has a large number of identical adsorption sites. Liquid molecules can attach to or detach from these sites, and there are energy barriers associated with this process.

Let us consider bitumen molecule displacing water from the glass surface. The number of times this occurs in unit time along unit length of contact line is K_b, which can be expressed through the theory of absolute reaction rates [16, 29]

$$K_b = \frac{k_B T}{h} \frac{Z^*}{Z_b} exp(\frac{-\epsilon_b}{k_B T}),$$

(3.8)

where k_B is the Boltzmann constant, T is the absolute temperature, h is the Planck's constant, Z^* and Z_b are statistical state functions for activated and initial states, ϵ_b is the activation energy for the displacement.

When the system is seemingly static, the frequencies of bitumen displacing water and water displacing bitumen are equal. Thus the wetting line fluctuates around its optimal position at a molecular scale.

$$K_b = K_w = k^0$$

(3.9)

$$\frac{k_B T}{h} \frac{Z^*}{Z_b} exp(\frac{-\epsilon_b}{k_B T}) = \frac{k_B T}{h} \frac{Z^*}{Z_w} exp(\frac{-\epsilon_w}{k_B T})$$

However, when apparent contact angle differs from the static value, unbalanced Young's force puts work into the system ($W = \gamma_{BW}(cos(\pi-\theta_S)-cos(\pi-\theta))$). Such work alters corresponding energy barriers for the displacement events (bitumen displacing water and water displacing bitumen), and contact line moves towards a new equilibrium position. Considering equation 3.9 and expression for W, the net frequency of displacement events can be expressed as

$$K_{net} = \frac{k_B T}{h}\frac{Z^*}{Z_b}exp(\frac{W\lambda^2 - \epsilon_b}{k_B T}) - \frac{k_B T}{h}\frac{Z^*}{Z_w}exp(\frac{-W\lambda^2 - \epsilon_w}{k_B T})$$

$$= K_b\ exp(\frac{W\lambda^2}{k_B T}) - K_w\ exp(\frac{-W\lambda^2}{k_B T})$$

$$= 2k^0 sinh(\frac{\gamma_{BW}(cos(\pi-\theta_S) - cos(\pi-\theta))\lambda^2}{k_B T}) \qquad (3.10)$$

By multiplying the net frequency of displacement (K_{net}) with typical distance between adsorption sites (λ), we obtain the relationship for the wetting line velocity

$$U = 2\,k^0\,\lambda\,sinh(\frac{\gamma_{BW}\,(cos(\pi-\theta_S) - cos(\pi-\theta))\lambda^2}{2\,k_B\,T}) \qquad (3.11)$$

In molecular-kinetic theory, energy dissipated at the contact line is measured with wetting line friction coefficient ($\zeta = \frac{k_B T}{k^0\lambda^3}$), and viscous dissipation in bulk liquid is considered negligible.

3.4 Combined Model

Combined molecular-hydrodynamic model is a unified consideration of both hydrodynamic flow and molecular processes at the three phase contact line. Here capillary forces drive liquid-liquid interface towards its equilibrium configuration, while excess energy is lost due to both hydrodynamic dissipation and wetting line friction. If we adopt de Gennes [10] view of dynamic partial wetting, then spontaneous displacement is driven by uncompensated Young's force ($F = \gamma_{SW} - $
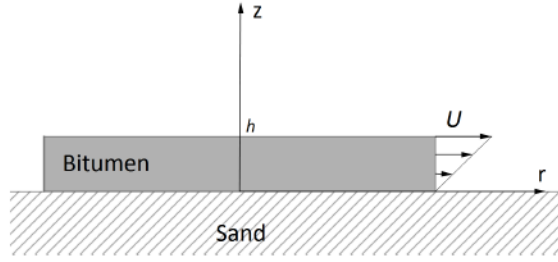
FIGURE 3.2: Simplified geometry of bitumen flow on solid surface. The droplet is substituted by liquid cylinder of equivalent size and volume

$\gamma_{BW} cos(\pi - \theta) - \gamma_{SB})$, and overall dynamics of oil droplet relaxation can be described by

$$FU = \dot{E}_l + \dot{E}_w \tag{3.12}$$

where $\dot{E}_l$ is the wetting line friction loss per unit length of contact line, and $\dot{E}_w$ is viscous dissipation in bulk liquid per unit length of contact line.

The dissipative contribution at the contact line $\dot{E}_l$ can be estimated from molecular-kinetic theory of Blake and Haynes [16]. Proposed relationship [11] at low capillary numbers is

$$\dot{E}_l = \zeta [\frac{dL(t)}{dt}]^2, \tag{3.13}$$

where $\zeta = \frac{k_B T}{k^0 \lambda^3}$ is the coefficient of wetting line friction.

The second dissipative contribution $\dot{E}_w$ comes from hydrodynamic consideration of the problem. Here we make use of de Ruijter et al. [30] view of droplet relaxation to obtain an expression for $\dot{E}_w$. Viscous dissipation in oil droplet is estimated considering quasi-steady Couette flow of a cylindrical liquid disk of identical size $L(t)$ and volume (Figure 3.2). The velocity profile for this flow can be written as $V(r, z) = C\frac{z}{r}$, where C is a constant. By imposing that the top edge of the liquid cylinder moves with the same speed as the speed of the droplet wetting line U, we obtain [30]

$$V(r, z) = \frac{dL(t)}{dt} \frac{L(t)}{h} \frac{z}{r} \tag{3.14}$$

Then the viscous energy dissipation rate per unit length of the contact line can be expressed as

$$\dot{E}_w = \frac{\mu_b \int_0^{2\pi} \int_{L_m}^{L(t)} \int_0^h r(\frac{\partial V(r,z)}{\partial z})^2 dz dr d\beta}{2\pi L(t)}$$

$$= 3\mu_b \phi [\frac{dL(t)}{dt}]^2 ln(\frac{L(t)}{L_m}) \tag{3.15}$$

where

$$\phi = \frac{(\frac{\pi}{2} - \alpha)^4}{sin\alpha} / \Big(\frac{cos^3\alpha}{cos^3(\alpha + \theta)} [2 + 3sin(\alpha + \theta)$$

$$- sin^3(\alpha + \theta)] + [2 - 3sin\alpha + sin^3\alpha] \Big)$$

originates from equality of bitumen droplet volume (3.1) to volume of the liquid cylinder under consideration.

Combining equations 3.12, 3.13 and 3.15, and considering negative direction of motion lead to the final expression for the combined molecular-hydrodynamic droplet relaxation model, which is nearly identical to the similar relations reported in literature [11, 30]

$$U = \frac{dL(t)}{dt} = \frac{\gamma_{BW} (cos(\pi - \theta_S) - cos(\pi - \theta))}{\zeta + 3\mu_b \phi ln(\frac{L(t)}{L_m})}. \tag{3.16}$$

In this relationship, the numerator represents the driving force for bitumen recession, while ζ and $\mu_b \phi ln(\frac{L(t)}{L_m})$ are the rate-limiting energy dissipation factors from the simplified molecular-kinetic and hydrodynamic approaches. If we neglect one of the dissipation mechanisms over another, the combined model reduces to either hydrodynamic or linearized molecular-kinetic models. When $\zeta \gg 3\mu_b \phi ln(\frac{L(t)}{L_m})$, the hydrodynamic expression can be safely neglected and equation (3.16) reduces to linear molecular-kinetic model developed by Blake and Haynes [16]. In the other extreme, equation (3.16) does not account for the wetting line friction losses and turns into the hydrodynamic model [19].

3.5 Solution Method

Temporal evolution of apparent contact angle can be obtained from combination of equation 3.3 and appropriate wetting line speed relation (equations 3.7, 3.11, or 3.16). The resulting expression is an ordinary differential equation, for which no analytic solutions are known. As a result, the theoretical contact angle temporal profiles must be obtained numerically.

A typical numerical solution can be demonstrated on the combined molecular-hydrodynamic formulation of droplet relaxation. Euler's numerical procedure is applied for demonstration purposes, and more accurate alternative methods are very similar in principle. The governing relation for the contact angle evolution is taken from equation 3.3

$$\frac{d\theta}{dt} = \frac{sin\theta(2 - sin(\theta + \alpha))}{r_m \, cos\alpha} \, U. \tag{3.17}$$

After substituting equation 3.16 into the above expression we obtain ordinary differential equation

$$\frac{d\theta}{dt} = -\frac{sin\theta(2 - sin(\theta + \alpha))}{r_m \, cos\alpha} \, \frac{\gamma_{BW}(cos\theta - cos\theta_S)}{\zeta + 3\,\mu_b\,\phi\,ln(\frac{L(t)}{L_m})}. \tag{3.18}$$

We should note that ϕ in the above expression is a functions of θ and α, both of which change as a function of time. In other words, we have two variables and only one equation. Hence, another relation must be introduced. Here equation 3.2 can be used to obtain the first derivative of angle α. The resulting system of ordinary differential equations is as follows.

$$\begin{cases} \frac{d\theta}{dt} = -\frac{sin\theta(2-sin(\theta+\alpha))}{r_m \, cos\alpha} \frac{\gamma_{BW}(cos\theta-cos\theta_S)}{\zeta+3\,\mu_b\,\phi\,ln(\frac{L(t)}{L_m})} = f_1(\alpha, \theta) \\[2mm] \frac{d\alpha}{dt} = \frac{1}{r_m} \frac{\gamma_{BW}(cos\theta-cos\theta_S)}{\zeta+3\,\mu_b\,\phi\,ln(\frac{L(t)}{L_m})} = f_2(\alpha, \theta) \end{cases} \tag{3.19}$$

Euler's form of numerical solution is obtained by applying finite difference approximation and making simple rearrangements to the above system.

$$
\begin{cases}
\theta_{i+1} = \theta_i + f_1(\alpha_i, \theta_i)\Delta t \\
\alpha_{i+1} = \alpha_i + f_2(\alpha_i, \theta_i)\Delta t
\end{cases}
\tag{3.20}
$$

Knowing initial values of θ and α, the solution can be propagated to a desired period in time. All of the alternative numerical solutions are similar in principle to Euler's method. In our study, contact angle profiles were obtained with Matlab's *ode45* solver, which utilized more accurate Runge-Kutta method. Numerical solutions were fitted to experimental data by optimizing values of either L_m in hydrodynamic model, or k^0 and λ in molecular-kinetic model, or L_m and ζ in combined model using the least square error method. The error between theoretical curve and experimental data was calculated as follows:

$$
Error\% = \frac{1}{n}\sum_{i=1}^{n}|\theta_{theoretical} - \theta_{experimental}|\frac{100}{\theta_S}
$$

where n was the number of experimental data points.

Chapter 4

Results and Discussion

4.1 Comparison of Dynamic Wetting Models

Before discussing a more specific case of oil sands liberation, we need to consider oil droplet recession in a more general sense. For this purpose, we examine the droplet recession in terms of capillary numbers. Capillary number measures the relative importance of viscous forces and interfacial tension acting along the liquid-liquid interface ($Ca = \frac{\text{viscous effect}}{\text{capillary effect}} = \frac{\mu_b U}{\gamma_{BW}}$). It is a dimensionless number, and hence most of the observations that we make here can be extended to other wetting systems by analogy.

In our typical oil recession experiment, wetting line moved rapidly at early stages and slowed down when contact angle approached its equilibrium value. Therefore capillary number dropped from its maximum value to zero as the droplet neared its optimal shape, and the typical capillary number profile would look like curve (a) in Figure 4.1. Greater values of capillary number were achieved by keeping droplet's viscosity high while stimulating faster initial displacement rates. Indeed, this was possible by modifying micro-spherical glass wettability. Figure 4.1 shows three representative droplet recession curves, with (a) and (c) corresponding to slow and fast displacements respectively. Images on the right side of Figure 4.1 show early droplet shapes for each curve. It is interesting to note that droplet
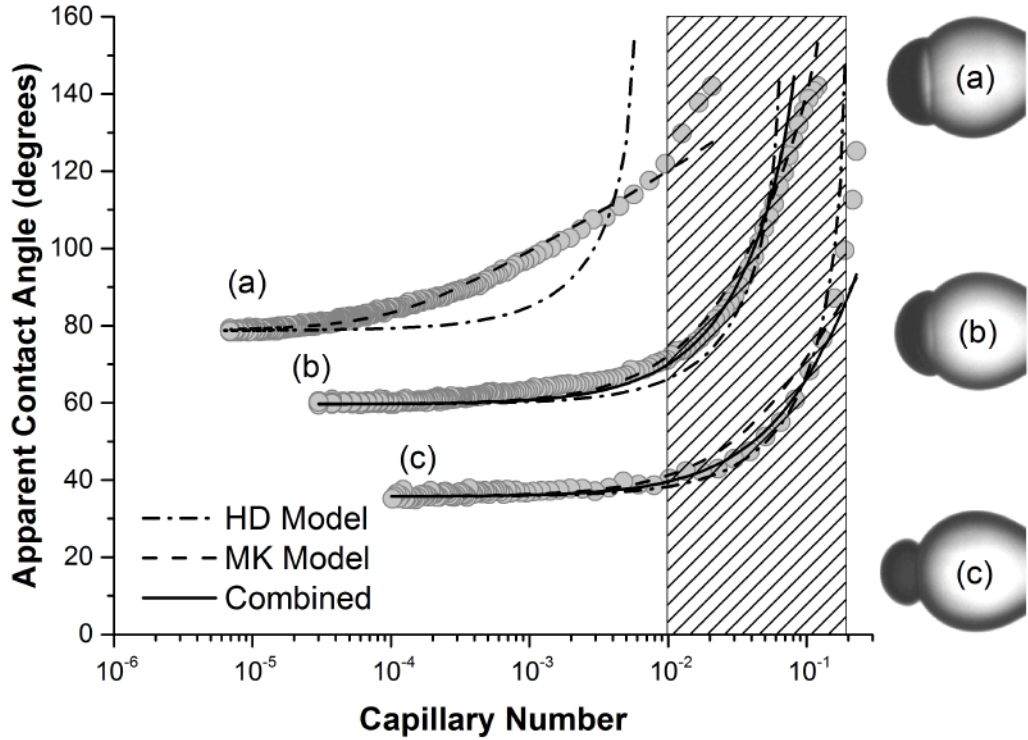
FIGURE 4.1: Apparent contact angle evolution profiles for oil droplet recession on glass substrates of different wettability. Hydrodynamic (HD), Molecular-Kinetic (MK), and Combined (CMB) models were fitted to experimental data with corresponding fitting parameters: (a) HD: $L_m = 3.1 * 10^{-51} m$; MK: $\zeta = 824 * \mu_b$; (b) HD: $L_m = 4.7 * 10^{-12} m$; MK: $\zeta = 20.2 * \mu_b$; CMB: $L_m = 2.92 * 10^{-5}$; $\zeta = 16.3 * \mu_b$; (c) HD: $L_m = 3.29 * 10^{-9} m$; MK: $\zeta = 5.9 * \mu_b$; CMB: $L_m = 5.2 * 10^{-6}$; $\zeta = 4.1 * \mu_b$.

shapes change from nearly spherical to perfectly spherical as the capillary number decreases. At high capillary numbers the droplet shape is significantly distorted from spherical shape due to viscous effect (image (c) in Figure 4.1).

It was our intention to study suitability of hydrodynamic, molecular-kinetic, and combined models over different ranges of capillary numbers. Suitability of one model over another would implicate that the wetting dynamics was dominated by one mechanism over the other. For example, if molecular-kinetic model was most appropriate for a particular experiment, then we could say that molecular-processes at the contact line define the rate of liquid-liquid displacement from the solid surface. Intuitively one could expect that significance of viscous dissipation

in the bulk liquid depends on the capillary number. At high capillary numbers, viscous forces are comparable to capillary forces, and thus one should expect significant viscous dissipation of energy. On the other hand, at very low capillary numbers viscous effects can be neglected, hence the energy is lost mainly at the contact line.

In fact, we can demonstrate that viscous dissipation alone is unlikely to control wetting rates at low capillary numbers. We should reinforce that in a typical hydrodynamic solution it is assumed that the liquid slips on the solid surface in the vicinity of the contact line. This means that if we calculated the viscous dissipation for the receding droplet, we would have no energy loss in the "slipping portion" of the oil droplet. In other words, the rate of oil recession is rate-limited by viscous dissipation in the bulk droplet, excluding the microscopic neighborhood (L_m) of the wetting line. Hydrodynamic fitting of experimental data in Figure 4.1 shows that for slow droplet recession (curve (a)) the slip length L_m would have to be as low as $3.1*10^{-51}$. However, the slip length values below molecular scale are deemed physically meaningless [10]. This means that viscous dissipation alone cannot account for three phase contact line displacement dynamics, and hydrodynamic description of wetting dynamics does not represents physics accurately at low capillary numbers.

Molecular-kinetic fitting, on the other hand, produced fair match to experimental data up to the capillary number of 10^{-2} (Figure 4.1). Fitting parameters k^0 and λ were within a reasonable range [11] for all contact angle profiles. At the same time, the wetting line friction coefficient value ζ drops from $824\mu_b$ in curve(a) to $5.9\mu_b$ in curve(c). This coefficient is a measure of energy losses due to molecular processes at the contact line. Parameter ζ has the same units as the viscosity, and can be used as a qualitative measure of relative importance of contact line energy losses and viscous dissipation. The friction coefficient of curve (a) is significantly greater than bitumen viscosity, which justifies neglecting viscous dissipation in bulk liquid over adsorption/desorption events. However, curve (c) produces ζ in the same order of magnitude as oil viscosity. This result indicates that hydrodynamic losses should not be neglected for capillary number range of experiment (c).

Moreover, in a system where adsorption-desorption mechanisms play a significant role in controlling the rate of wetting line motion, wetting line friction coefficient ζ can be linked with work of adhesion W_a. Blake and Coninck [31] proposed that the friction coefficient depends linearly on viscosity and exponentially on work of adhesion:

$$\zeta \approx \frac{\mu_b v_L}{\lambda^3} \, exp(\frac{W_a \lambda^2}{k_B T}), \tag{4.1}$$

where v_L is volume of flow unit. Hence, in a system where molecular-kinetic description of wetting applies, experimental values of W_a versus $ln(\zeta)$ should follow a straight line.

In fact, Figure 4.2 shows the plot of $ln(\zeta)$ against work of adhesion, where the friction coefficient was obtained from molecular-kinetic fitting of experimental data. Indeed, all of the experiments in Figure 4.2 conform to a straight line, with few interesting exceptions. Two of the wettability points that deviated from the straight line result from curves (b) and (c) in Figure 4.1. This deviation could be attributed to a sudden decrease in magnitude of $\frac{\mu_b v_L}{\lambda^3}$ in equation (4.1). This change would need to be at least five-fold in order to bring wettability points (b) and (c) back to the straight line. However, values of λ were very similar for all experimental points in Figure 4.2, and thus λ could not account for the observed deviation. Similarly, there is no apparent indication that the flow unit volume v_L should change so abruptly. One of the plausible explanations could be that during the bitumen recession energy dissipation within the droplet turned into heat and decreased the viscosity significantly. However, Moran and Yeung [32] demonstrated that during a micron-scale bitumen droplet relaxation in aqueous solutions dissipative heat is transported entirely to the surroundings. Hence, it is safe to assume that both temperature and viscosity of the bitumen droplet remain constant during the recession. As a result, apparent deviation of two wettability points from the straight line could be yet another indication that molecular-kinetic description is not the only rate-limiting factor at high capillary numbers. Similarly, we could explain the deviation of point "pH11" in Figure 4.2 by the fact that significant portion of its contact angle evolution profile lies above capillary number of 10^{-2}, much like curves (b) and (c) in Figure 4.1.
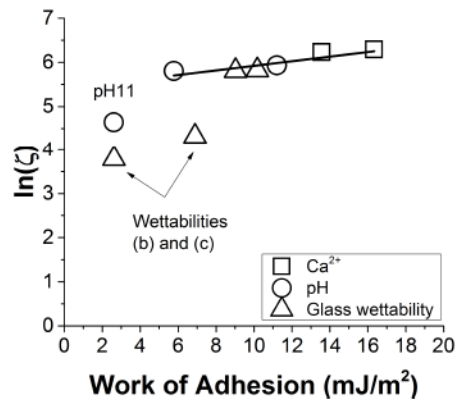
FIGURE 4.2: Plot of $ln(\zeta)$ vs. W_a. In bitumen-water-glass system the work of adhesion is given by $\gamma(1 - cos\theta_S)$, when apparent contact angle is measured from the water phase

As a result, a combination of hydrodynamic and molecular-kinetic models should be considered at higher capillary numbers. Let us return to a typical behaviour of receding bitumen droplet. Once bitumen-coated substrate is placed in aqueous solution, the droplet recession starts relatively quickly and slows down as it gets closer to optimal shape. Thus, at early stages one should expect considerable viscous dissipation in oil phase. Hydrodynamic losses gradually decrease until they eventually become negligible, where adsorption/desorption mechanisms dominate wetting line velocity. Hence, whenever considerable portion of dynamic contact angle profile has capillary numbers above 10^{-2}, both hydrodynamic and molecular processes have significant control over the wetting rates. As a result, combined molecular-hydrodynamic model produces closer match to curves (b) and (c) in Figure 4.1, generating reasonable fitting parameters. The increasing importance of viscous effects can also be visually demonstrated in our micro-scale displacement tests. Images on the right side of Figure 4.1 correspond to early shapes of bitumen droplets for experiments (a) to (c) respectively. We can see that experiments that start at high capillary numbers experience a higher degree of viscous bending near the three phase contact line, which implies a higher viscous dissipation in oil phase.

This approach was used as a guide when selecting dynamic wetting model to be implemented. Whenever significant portion of the temporal contact angle had capillary numbers below 10^{-2}, molecular-kinetic approach was taken to interpret

the results. In all of the other cases, a combination of molecular-kinetic and hydrodynamic models was used to fit the experimental data.

4.2 Factors Influencing Bitumen Liberation

4.2.1 Effect of Substrate Wettability

Hydrophilic nature of solids in Athabasca oil sands made it possible to recover bitumen utilizing Clark and Pasternack [3] hot water-based extraction process. When solids have high affinity to water, bitumen can be easily removed from the solid surface when oil sands are mixed with water. On the other hand, if solids were more hydrophobic in nature, it would take a great deal of effort to displace bitumen from the solid surface.

In our experimental setup, freshly prepared (freshly melted and solidified) micro-spherical glass substrates had only slightly higher affinity for water than for bitumen. This was reflected in the static contact angle of 78°, measured from the water phase. Glass surface was less hydrophilic due to the removal of the hydroxide surface layer during the glass transition portion of substrate fabrication. Therefore, this slightly hydrophilic glass substrate was a good starting point to investigate the effect of wettability on wetting line displacement dynamics.

By placing freshly fabricated substrates into the aqueous solution of pH 8.3, we were able to increase substrates' affinity to water by surface hydrolysis. When glass was placed in aqueous solutions, its surface was hydrolyzed and deprotonated [2]. This made the glass surface more negatively charged, and thus more hydrophilic in nature [33]. The longer the glass was exposed to water, the higher was its affinity to aqueous phase. Each micro-spherical tip was then dried in a clean fume-hood environment for several hours prior to bitumen coating. The dynamic wetting experiments were performed with fixed bitumen and water phases at room temperature. It should be noted that the wettability of glass sphere can be estimated in-situ, at the end of the dynamic displacement experiments.
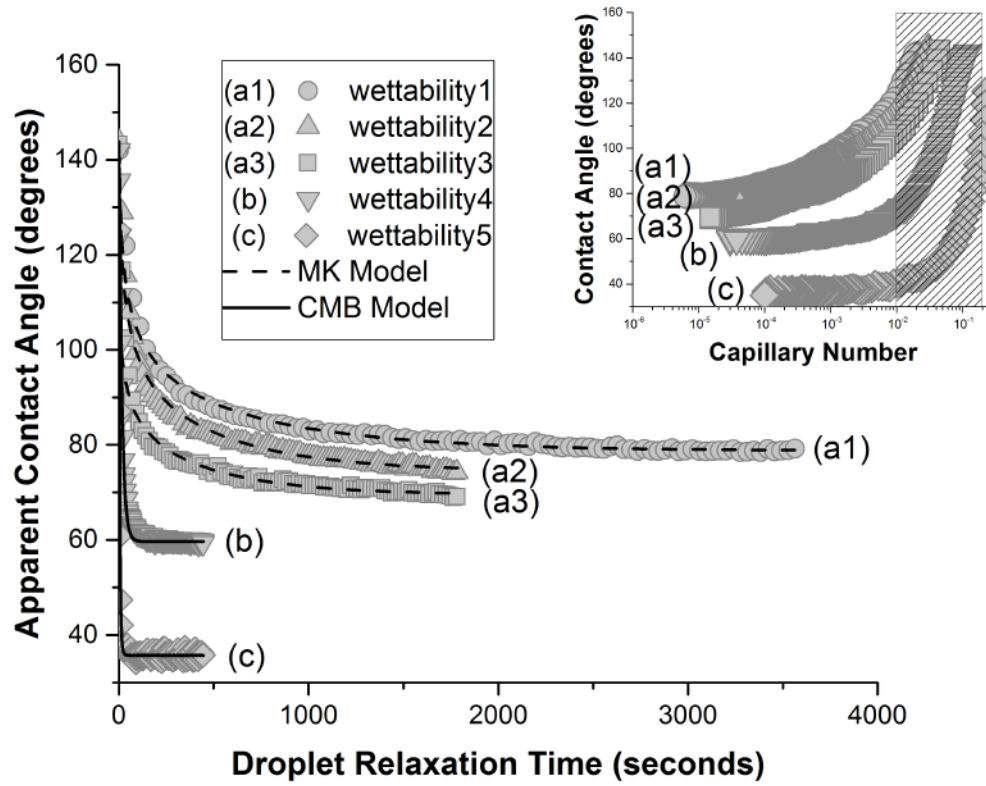
FIGURE 4.3: Effect of glass wettability on bitumen droplet recession. The experimental curves are arranged in increasing degree of substrate hydrophilicity from (a) to (c). Droplet relaxation fitting parameters: (a1) MK: $\zeta = 824 * \mu_b$; (a2) MK: $\zeta = 641 * \mu_b$; (a3) MK: $\zeta = 619 * \mu_b$; (b) CMB: $L_m = 2.92 * 10^{-5}$, $\zeta = 16.3 * \mu_b$; (c) CMB: $L_m = 5.2 * 10^{-6}$, $\zeta = 4.1 * \mu_b$;

In each of the displacement experiments, dynamic contact angle changed rapidly at early stages of the experiment and slowed down when approaching to a static value. Wetting line velocity showed a strong connection with substrate wettability: bitumen droplets receded faster on more hydrophilic surfaces as anticipated. Figure 4.3 shows contact angle evolution in increasing degree of substrate hydrophilicity from (a) to (c). Since water and bitumen phases were kept constant from one experiment to another, the only factor that changed was the strength of solid-liquid interactions at the contact line. Hence, it is only reasonable that the resistance to flow at the contact line decreased sharply when substrate's affinity to water increased.

The curves (a1) to (a3) in Figure 4.3 reached their equilibrium contact angles at capillary numbers much smaller than 10^{-2}. This observation indicates that the

displacement dynamics of (a1) to (a3) is mostly governed by molecular-kinetic mechanisms, according to our findings in section 4.1. The curves (b) and (c), on the other hand, have a significant portion of their temporal contact angles at higher capillary numbers, and thus both hydrodynamic and molecular-kinetic dissipation mechanisms have significant effect on the displacement rates. Therefore, molecular-kinetic model provides

Theoretical fitting of the experimental data in Figure 4.3 shows that the coefficient of wetting line friction dropped from $824 * \mu_b$ in curve (a1) to $4.1 * \mu_b$ in curve (c). Therefore, we find that the resistance to displacement of the three phase contact line drops dramatically as the solid's affinity to aqueous phase increases. It is clear that reaching or maintaining the hydrophilic nature of the solid is a key in achieving high rate and degree of bitumen liberation from sand grains.

4.2.2   Effect of pH

It is commonly believed that increasing pH of the oil sand slurry assists in faster liberation of bitumen phase from solids in Athabasca oil sands. Increasing aqueous solution pH modifies both bitumen-water and glass-water interfaces.

Higher pH values aid ionization and accumulation of natural surfactants at bitumen-water interface [2]. This reduces bitumen-water interfacial tension γ_{BW}, which was verified with our drop shape recovery tests (Table 2.1).

Increased concentration of the OH^- group in aqueous solution also triggers higher degree of deprotonation of hydrolyzed substrate surface. The glass surface accumulates additional negative charges [2]. Hanly et al. [34] demonstrated that when solid surface carries a charge, solid-liquid specific free energy can be divided into two contributing components:

$$\gamma_{SW} = \gamma_{SW}^o + \Delta F_{dl} \tag{4.2}$$
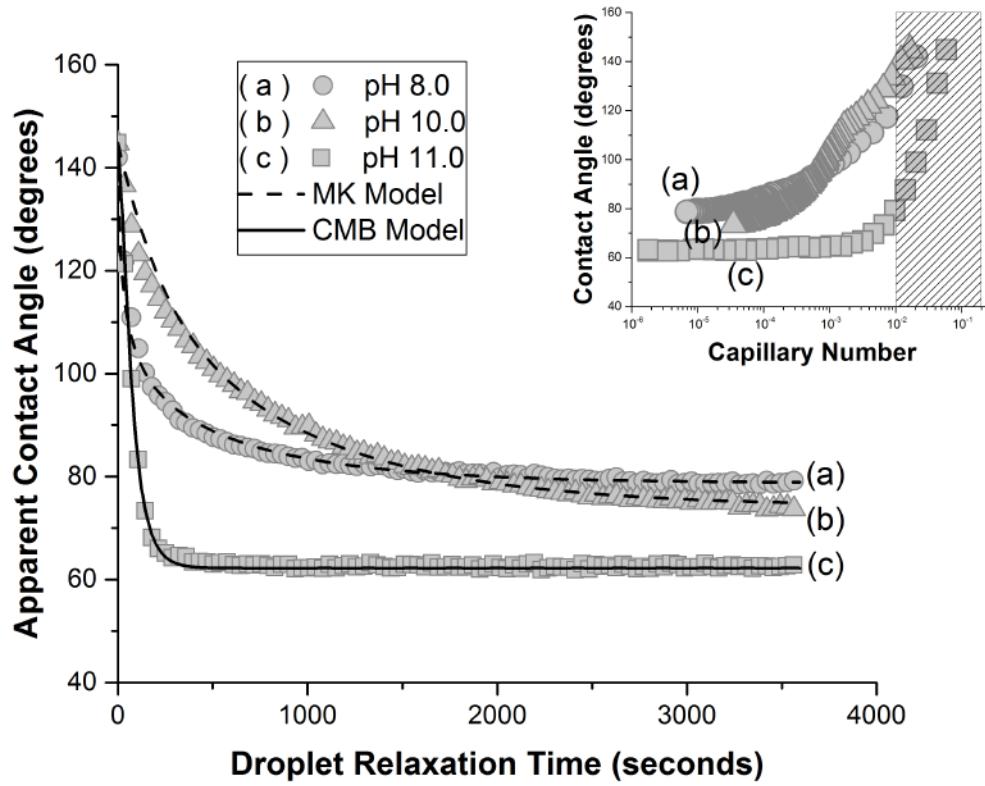
FIGURE 4.4: Effect of pH on apparent contact angle evolution. Molecular-kinetic model was fitted to experimental observations with: (a) $\zeta = 824 * \mu_b$ at pH 8.0 (b) $\zeta = 617 * \mu_b$ at pH 10.0 (c) $\zeta = 27.5 * \mu_b$; $L_m = 1.5 * 10^{-5}$ at pH 11.0

where γ_{SW}^o is the interfacial tension at point of zero charge, and ΔF_{dl} represents the free energy of formation of the ionizable surface relative to the point of zero charge [34]. In the simplest case of constant and low potential, the energy that goes into formation of electric double layer around charged interface can be expressed as:

$$\Delta F_{dl} = -\frac{1}{2}\epsilon\epsilon_o\kappa\psi_o^2. \tag{4.3}$$

It is important to note that ΔF_{dl} is always negative. The electric double layer forms spontaneously, and thus specific free energy of the interface reduces whenever it carries charges. Therefore, solid-water interfacial tension γ_{SW} reduces as the glass accumulated more negative charges.

Reduced values of γ_{BW} and γ_{SW} contribute to increase in $cos\theta_S = \frac{\gamma_{SB}-\gamma_{SW}}{\gamma_{BW}}$. This means that the work of adhesion of bitumen and solid in water environment ($W_a =$

$\gamma_{BW}(1-cos\theta_S)$) also reduces. According to our observations in section 4.1, weaker work of adhesion between bitumen and solid should also trigger lower friction losses at the contact line. As expected, Figure 4.4 shows that the wetting line friction coefficient reduces with higher values of pH. The diagnostic capillary number plot in Figure 4.4 shows that the displacement rates at pH values of 8 and 10 are mostly governed by molecular-kinetic dissipation, while at pH 11 viscous dissipation in bulk liquid also plays an important role. The physical importance of this finding is that at higher pH (and higher capillary numbers), the displacement dynamics could also depend on the size of the droplet, while at lower pH the displacement rates are independent of the scale.

The shape transition of the contact angle profiles from pH 8 to 11 is noteworthy and we shall discuss it in a little more detail. As we mentioned in section 3.3, the driving force for the wetting line motion is an unbalanced Young force ($\gamma_{BW}(cos(\pi - \theta_S) - cos(\pi - \theta))$). The rate-limiting factor is the wetting line friction coefficient. As we increased the pH from 8 to 10, interfacial tension and thus the driving force reduced by about 43%. At the same time, the wetting line friction coefficient dropped by only about 25%. As a result, even though the contact angle decreased, it took longer for the droplet to reach its optimal shape. On the other hand, when pH increased from 10 to 11, the resistance to flow decreased much faster than the driving force. As a result, the overall dynamics of the droplet recession was faster for pH 11.

4.2.3   Effect of $CaCl_2$

Much like the effect of solution pH, the presence of Ca^{2+} ions modifies both bitumen-water and glass-water interfaces. Compared with the effect of pH however, the change is in the opposite direction.

Ca^{2+} ions reduce the concentration of natural surfactant at the bitumen-water interface, and thus increase bitumen-water interfacial tension, as shown in our interfacial tension measurements in Table 2.1.
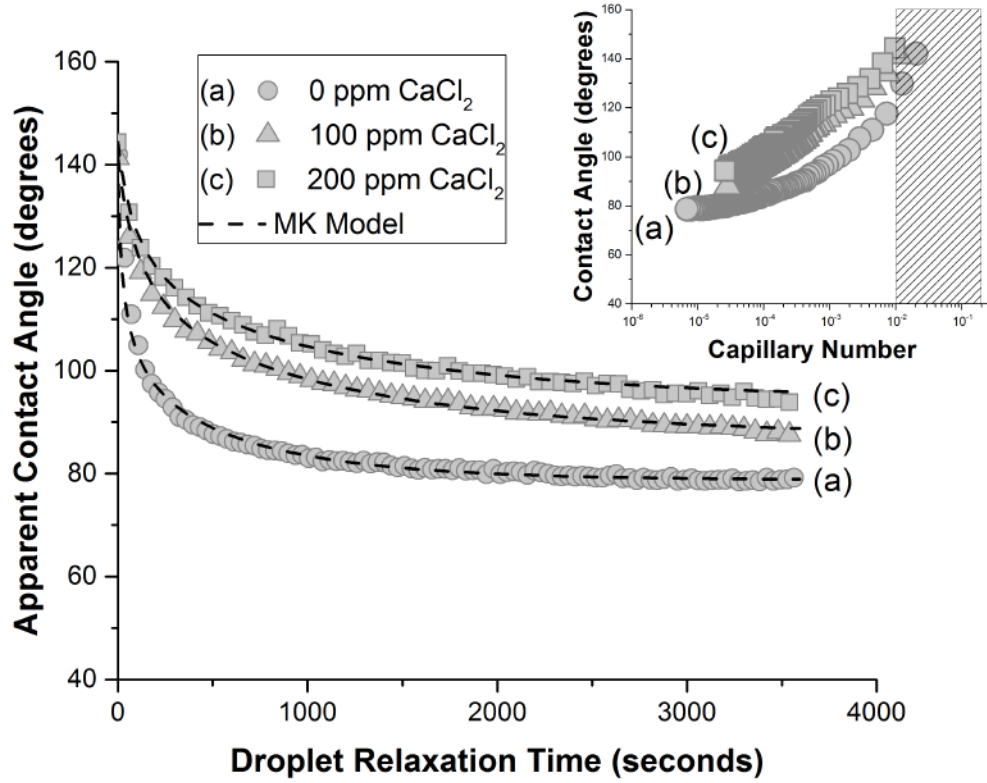
FIGURE 4.5: Effect of $CaCl_2$ concentration in aqueous phase on apparent contact angle evolution. Molecular-kinetic model was fitted to experimental observations with: (a) $\zeta = 824 * \mu_b$ at 0ppm $CaCl_2$; (b) $\zeta = 1648 * \mu_b$ at 100ppm $CaCl_2$; (c) $\zeta = 1902 * \mu_b$ at 200ppm $CaCl_2$

Moreover, at solution pH of 8 and above, calcium monohydroxy ions ($CaOH^+$) adsorb on hydrolyzed silica surface (SiO^-) forming covalent $SiOCa$, reducing the overall negative charge of the substrate [2]. The reduced charge of silica surfaces due to presence of Ca^{2+} ions was experimentally confirmed by Liu et al. [35] for a similar environment. As it was demonstrated with equations (4.2) and (4.3), reduced charges on the solid surface increase solid-liquid interfacial tension.

As a result, we should expect that addition of Ca^{2+} ions increases the static contact angle, since $cos\theta_S = \frac{\gamma_{SB} - \gamma_{SW}}{\gamma_{BW}}$. This is in fact confirmed by our droplet recession experimental results in Figure 4.5.

All of the temporal contact angle profiles in Figure 4.5 had much of their associated capillary numbers below 10^{-2}, and therefore the displacement rates were governed by molecular-kinetic model. The model produced good fit to experimental data,

and wetting line friction increased from $824\mu_b$ to $1902\mu_b$ with increasing $CaCl_2$ concentrations to 200ppm. This finding confirms that the addition of calcium ions to aqueous phase changes bitumen-water and glass-water interfaces increasing the resistance to three-phase contact line motion.

4.2.4   Effect of $NaCl$

In the industrial oil sands extraction plants, the process water is recycled many times with only small portion of fresh water added in each cycle. During each recycle, the water pH is adjusted by the addition of $NaOH$. As a result, the concentration of the sodium ions can build up to very high values during the lifetime of the extraction plant. Takamura and Wallace [36] showed that bitumen recovery can drop by as much as 45% when Na^+ ion concentration reaches 1725ppm. This was also confirmed by Basu et al. [37], although he had to go up to much higher concentration of sodium ions before he observed detrimental effects. Moreover, Basu et al. [37] noticed that wetting dynamics is affected much more at higher values of pH. All of this observations can be explained with the understanding of wetting developed in this thesis.

At aqueous solution pH of 8, sodium ions establish the electric double layer around negatively charged bitumen-water and glass-water interfaces. The incremental concentrations of Na^+ reduce the Debye length and increase the absolute value of ΔF_{dl} in equation (4.2). This means that both γ_{BW} and γ_{SW} decrease, and the static contact angle reduces. However, the changes to the interface free energy are rather small, and hence not easily observed in droplet recession experiments. All three of the contact angle profiles in Figure 4.6 overlap almost entirely, and differences between the curves are certainly within the error of the experimental method.

All three of the displacement experiments reach their equilibrium contact angles at capillary number much smaller than 10^{-2}. As a result, they all produce a good fit to molecular-kinetic model, and most of the energy dissipation happens in the
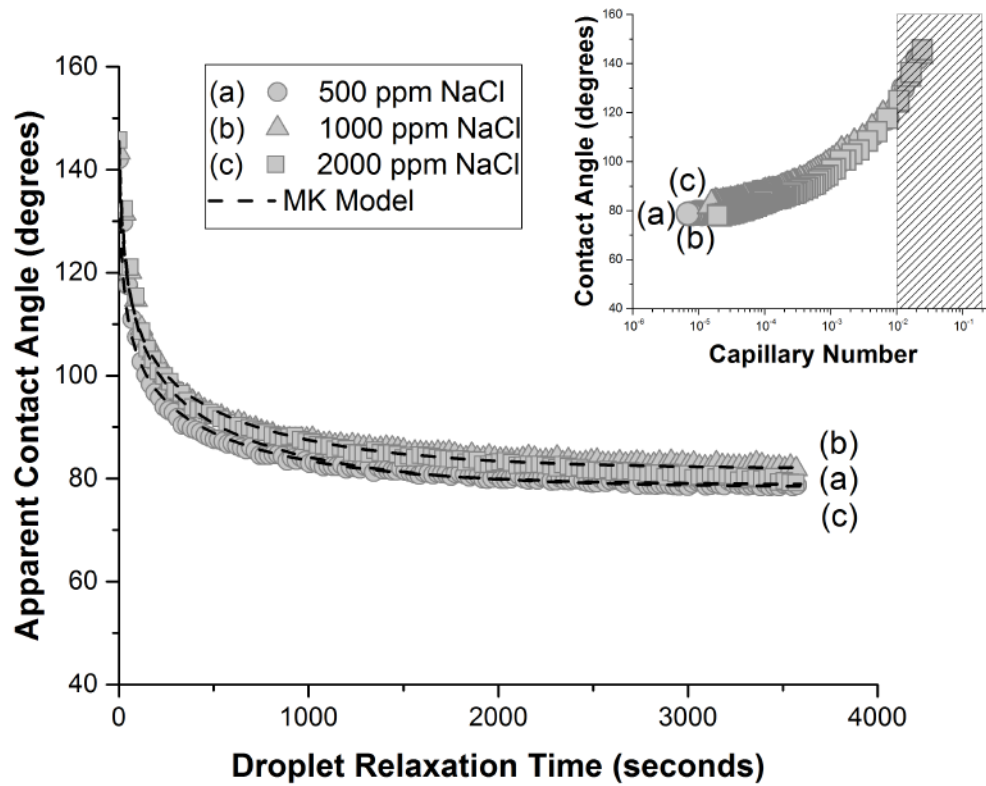
FIGURE 4.6: Effect of $NaCl$ concentration in aqueous phase on apparent contact angle evolution. Molecular-kinetic model was fitted to experimental observations with: (a) $\zeta = 824 * \mu_b$ at 500ppm NaCl; (b) $\zeta = 650 * \mu_b$ at 1000ppm NaCl; (c) $\zeta = 619 * \mu_b$ at 2000ppm NaCl

immediate neighborhood of the three-phase contact line. All three curves in Figure 4.6 produce the wetting line friction coefficient of the same order of magnitude. Therefore, we can conclude that the changes in sodium ion concentrations have insignificant effect on bitumen displacement rates at pH value of 8.

4.2.5 Effect of Temperature

In all of the previous sections, only system's interfacial properties were modified and bitumen viscosities were kept constant. However, reducing the liquid viscosity can be another powerful tool to aid bitumen liberation. The current mineable oil sands extraction process runs at about 50°C, at which point bitumen flows easily.
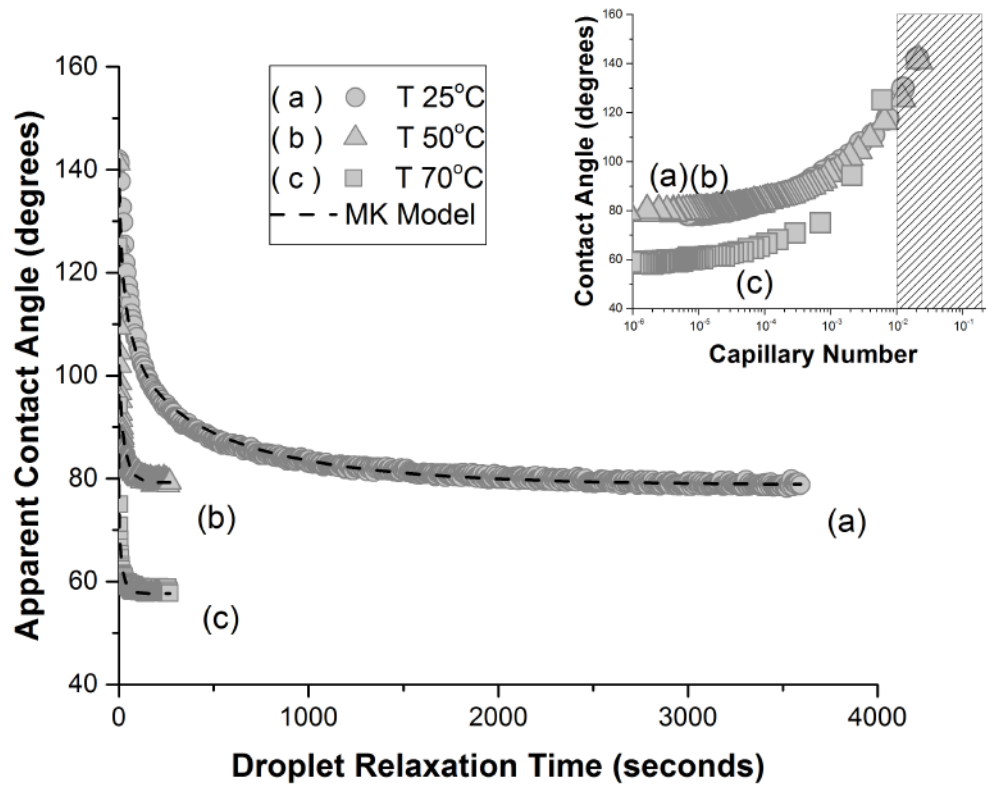
FIGURE 4.7: Effect of temperature on apparent contact angle evolution. Molecular-kinetic model was fitted to experimental observations with: (a) $\zeta = 824 * \mu_b$ at 25°C; (b) $\zeta = 46 * \mu_b$ at 50°C; (c) $\zeta = 24 * \mu_b$ at 70°C

Figure 4.7 shows the temporal contact angles of bitumen droplets at $25°C$, $50°C$ and $70°C$. All three curves have associated capillary numbers below 10^{-2}, and therefore the displacement dynamics is controlled by adsorption/desorption events at the three phase contact line. As shown in Figure 4.7, the experimental results fit very well by molecular-kinetic model.

Bitumen viscosity reduces exponentially as its temperature goes up, which was confirmed by our viscosity measurements (Figure 2.4). Lower viscosity values mean the wetting line friction coefficient ζ reduces, as it is directly proportional to viscosity (see equation 4.1). As a result, the droplet receded significantly faster from the glass surface at higher temperatures (Figure 4.7). As expected, the wetting line friction coefficient decreased exponentially with increasing temperature, following the trends of bitumen viscosity.

It is important to note that when the silica surface is not fully hydrolyzed, which was the case in our micro-pipette experiments, high temperature of aqueous phase could accelerate hydrolysis and deprotonation of the substrate. As a result, the solid would become more hydrophilic, and static contact angle would decrease, which was observed for our droplet recession experiments at 70°C.

Moreover, higher solution temperature modifies the bitumen-water interfacial tension. However, these changes are not always straightforward and the interfacial tension measurements become rather difficult to perform. This offers a window of opportunity for future research, given that a temperature controller is added to current experimental setup.

4.2.6 Effect of Diluent Addition

The industrial-scale hot water-based bitumen extraction process does involve large quantities of process water. Keeping the process at 50°C can be energy intensive, and therefore costly.

An alternative solution for reducing the bitumen viscosity could be soaking bitumen in a diluent before processing it in the extraction plant. Diluents are indeed used in large quantities at late stages of bitumen extraction, and the process could be implemented at an industrial scale. The effectiveness of the hybrid process was demonstrated on poor processing ore by the laboratory scale tests [38]. Addition of 15% diluent has shown to improve the bitumen recovery from 35% to 90%. These findings are further reinforced by our bitumen droplet displacement experiments (Figure 4.8).

It was shown that the addition of naphtha as a diluent can be as effective as a temperature increase to reduce bitumen viscosity [19, 39]. The viscosity value drops several orders of magnitude when adding just 10wt% of naphtha, and it goes as low as about $0.4 Pa * s$ at 30wt% of naphtha addition. As a result, the resistance to bitumen recession on solid surface reduces significantly.
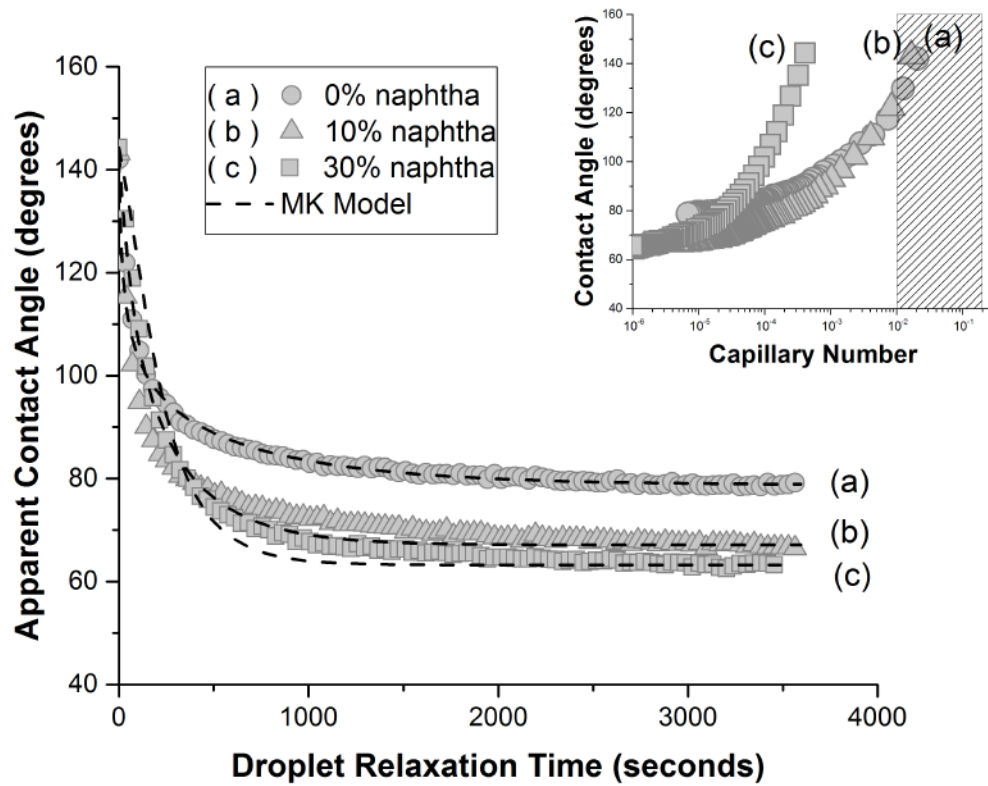
FIGURE 4.8: Effect of naphtha addition on apparent contact angle evolution. Molecular-kinetic model was fitted to experimental observations with: (a) $\zeta = 824 * \mu_b$ at 0% naphtha; (b) $\zeta = 12.8 * \mu_b$ at 10% naphtha; (c) $\zeta = 2.4 * \mu_b$ at 30% naphtha

However, addition of naphtha to bitumen also reduces bitumen-water interfacial tension. The interfacial tension drops by a factor of 10 when just 10wt% of naphtha is present [19, 39]. The reduction in interfacial tension by bitumen dilution with naphtha reduces the driving force of bitumen droplet displacement, as shown in unbalanced Young force. Hence, compared with the effect of temperature, naphtha has slightly smaller effect on improving the rate of bitumen liberation. The droplet recession tests in Figure 4.8 show that bitumen is displaced faster from the glass surface when 10wt% of naphtha is added, with only slight further improvement at 30wt% of naphtha addition. It should also be noted that the experimental results with naphtha addition does not fit with the molecular-kinetic model as well as in the case of increasing temperature.

4.3 Rate-Defining Parameters of Bitumen Liberation

In the above sections, we established that modifying the water phase chemistry as well as reducing the bitumen viscosity can be an effective tool to enhance bitumen liberation rates. We also demonstrated that the displacement rates are proportional to the magnitude of unbalanced Young force and limited by viscous dissipation and wetting line friction losses. In most general cases, the overall dynamics of the bitumen droplet recession can be described by equation (3.16)

$$U = \frac{\gamma_{BW}(cos(\pi - \theta_S) - cos(\pi - \theta))}{\zeta + 3\,\mu_b\,\phi\,ln(\frac{L(t)}{L_m})}.$$

Since the wetting line friction coefficient ζ is directly proportional to the liquid viscosity, we can factor out the term $\frac{\gamma_{BW}}{\mu_b}$ from the above equation.

$$U = \frac{\gamma_{BW}}{\mu_b}\frac{cos(\pi - \theta_S) - cos(\pi - \theta)}{\zeta/\mu + 3\,\phi\,ln(\frac{L(t)}{L_m})}.$$

The above equation can then be used as a guide in designing optimal conditions for bitumen liberation. Ideally, we would want to have a substantial driving force and small magnitudes of the rate-limiting factors. This could be done by having greatest possible value for $\frac{\gamma_{BW}}{\mu_b}$ and maintaining lowest possible static contact angle θ_S.

Chapter 5

In-Situ Bitumen Recovery

5.1 Model of Fluid Flow in Porous Media

The ideas developed in chapters 3 and 4 can be extended beyond hot water based oil sands extraction applications. The immiscible fluid-fluid displacement from the solid surfaces also takes place in in-situ oil recovery. Therefore, the physics involved in in-situ recovery and bitumen liberation is much alike. We use an approach very similar to the combined droplet recession model in chapter 3 to describe slow displacement of one liquid by another in a capillary tube. This model is an extension to a Washburn equation, and can be used to model performance of SAGD and conventional oil recovery.

5.1.1 Dynamic Wetting of Capillary Tube

Fluid flow distribution inside the capillary tube can be obtained from the Navier-Stokes equation with few simplifying assumptions. Let us consider immiscible Newtonian fluid-fluid displacement in a capillary tube with inner radius of R (Figure 5.1). We assume that the flow is incompressible and viscosity of one fluid is much higher than the viscosity of the other fluid, and momentum is only transported along the z-axis in Figure 5.1. Then, the corresponding component of
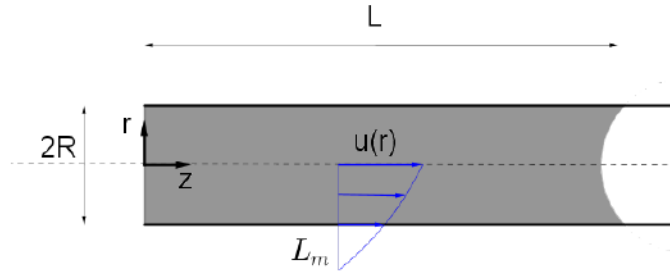
FIGURE 5.1: Schematic view of immiscible fluid displacement in a capillary tube

the Navier-Stokes equation is [40]

$$\rho(\frac{\partial u}{\partial t} + u_r\frac{\partial u}{\partial r} + \frac{u_\phi}{r}\frac{\partial u}{\partial \phi} + u\frac{\partial u}{\partial z}) = -\frac{\partial p}{\partial z} + \mu(\frac{1}{r}\frac{\partial}{\partial r}(r\frac{\partial u}{\partial r}) + \frac{1}{r^2}\frac{\partial^2 u}{\partial \phi^2} + \frac{\partial^2 u}{\partial z^2}). \quad (5.1)$$

The flow is axisymmetric ($\frac{\partial}{\partial \phi} = 0$), fully developed ($\frac{\partial u}{\partial z} = 0$) and at steady state ($\frac{\partial}{\partial t} = 0$). We also assume that the radial and swirl components of fluid flow are negligible ($u_\phi = u_r = 0$). Then, the Navier-Stokes equation reduces to

$$\frac{1}{r}\frac{\partial}{\partial r}(r\frac{\partial u}{\partial r}) = \frac{1}{\mu}\frac{\partial p}{\partial z}. \quad (5.2)$$

The fluid velocity distribution can be then written as

$$u(r) = \frac{1}{4\mu}\frac{\partial p}{\partial z}r^2 + c_1 ln(r) + c_2, \quad (5.3)$$

where c_1 and c_2 are the integration constants.

Considering that the fluid velocity is finite at $r = 0$, and that the slip on solid surface is defined as illustrated in Figure 5.1, we obtain the following relationship for the flow distribution:

$$u(r) = \frac{1}{4\mu}\frac{\partial p}{\partial z}r^2 - \frac{1}{4\mu}\frac{\partial p}{\partial z}(R + L_m)^2$$
$$= \frac{1}{4\mu}\frac{\partial p}{\partial z}(r^2 - R^2 - 2RL_m) \quad (5.4)$$

Then the speed of the wetting line can be expressed as the average flow velocity across the capillary cross section:

$$U = \frac{1}{\pi R^2} \int_0^R u(r)\, 2\pi r dr$$
$$= -\frac{1}{8\mu} \frac{\partial p}{\partial z}(R^2 + 4RL_m). \tag{5.5}$$

Combining equations (5.4) and (5.5), we obtain the equation of flow distribution in a capillary tube expressed through the speed of the wetting line U:

$$u(r) = -\frac{2(r^2 - R^2 - 2RL_m)}{R^2 + 4RL_m} U. \tag{5.6}$$

The governing relation for capillary wetting can be derived in a similar manner to oil droplet recession. The work done on the system is balanced by viscous dissipation in the bulk liquid $\dot{E}_w$ and the friction losses at the contact line $\dot{E}_l$. The overall dynamics of wetting can be conveyed with de Gennes [10] equation:

$$FU = \dot{E}_l + \dot{E}_w \tag{5.7}$$

However, in this case we do not assume that the flow is only driven by capillary forces, and we express the driving force in a more general way. The force per unit length of the contact line can be calculated through the sum of external pressure contributions $\sum P$:

$$F = \frac{\sum(P)\,\pi R^2}{2\pi R}$$
$$= \frac{\sum(P)\,R}{2} \tag{5.8}$$

Here, $\sum P$ consists of unbalanced external pressure, capillary pressure, and gravity contribution to pressure differences.

The rate of energy loss per unit length of the contact line is expressed with Blake [11] relationship:

$$\dot{E}_l = \zeta U^2. \tag{5.9}$$

The viscous dissipation per unit length of the contact line can be calculated utilizing the flow equation (5.6):

$$\dot{E}_w = \frac{\mu}{2\pi R} \int_0^{2\pi} \int_0^L \int_0^R r \left(\frac{\partial u(r)}{\partial r}\right)^2 drdzd\beta$$

$$= \frac{\mu}{2\pi R} \int_0^{2\pi} \int_0^L \int_0^R r \left(\frac{4r}{R^2 + 4RL_m} U\right)^2 drdzd\beta$$

$$= \frac{\mu}{2\pi R} \frac{8\pi L U^2}{(1 + \frac{4L_m}{R})^2}$$

$$= \frac{4\mu L U^2}{R(1 + \frac{4L_m}{R})^2} \tag{5.10}$$

By substituting relations (5.8)-(5.10) into the energy balance equation (5.7), we obtain the final relation for dynamic wetting in a capillary tube

$$U = \frac{\sum(P)\ R}{2\zeta + 8\mu L \frac{1}{R(1+4L_m/R)^2}} \tag{5.11}$$

This relationship is very similar to the combined model of droplet recession. The term in the numerator represents the driving forces for the flow, while two terms in denominator stand for rate-limiting factors due to viscous dissipation and wetting line friction. The equation (5.11) can be reduced to a more familiar form, given few simplifying assumptions.

5.1.2   Washburn Equation

When the friction losses at the wetting line are negligibly small compared to the viscous dissipation in the bulk liquid and $R \gg L_m$, the equation (5.11) reduces to

$$U = \frac{\sum(P)\ R^2(1 + 4L_m/R)^2}{8\mu L}$$

$$= \frac{\sum(P)\ (R^2 + 8L_m R + L_m^2)}{8\mu L}$$

$$= \frac{\sum(P)\ (R^2 + 8L_m R)}{8\mu L} \tag{5.12}$$

46

which is almost identical to Washburn [41] equation. In fact, when the value of the slip length can be neglected in comparison with the capillary radius, equation (5.12) reduces to the most commonly used form of Washburn equation.

$$\frac{dL}{dt} = \frac{\sum(P)\ R^2}{8\mu L} \tag{5.13}$$

The slip length is normally of a nanometer scale, and hence the above simplification is applicable to a wide range of liquid-solid systems.

Even though Washburn [41] relationships quantify the flow through a single capillary tube, it has been experimentally verified to be accurate for flow through porous media [42].

5.1.3 Darcy Equation

The fluid flow through porous media is most commonly quantified with Darcy's empirical relationship. Darcy experimentally observed that when the pressure differential is applied through the porous cylinder of length L and cross section A, the volume flow rate abides by expression

$$Q = -\frac{kA}{\mu}\frac{\Delta P}{L}, \tag{5.14}$$

where k is the rock permeability.

Rearranging terms in equation (5.12) allows direct comparison with the Darcy equation. If we assume that the flow is driven by external pressure differential, then $\sum(P) = -\Delta P$. The negative sign signifies that the flow is in the direction of the pressure drop. Thus, by multiplying both sides of the equation (5.12) by the "flow area" A, we obtain an equivalent of Darcy equation:

$$Q = -\left(\frac{(R^2 + 8L_m R)}{8}\right)\frac{A}{\mu}\frac{\Delta P}{L} \tag{5.15}$$

where $\frac{(R^2 + 8L_m R)}{8}$ is the measure of permeability.
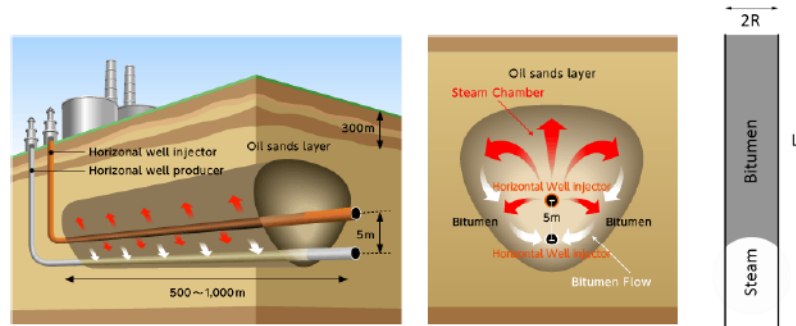
FIGURE 5.2: Schematic representation of SAGD process. The image on the right represents a schematic SAGD process in a single capillary tube. The two images on the left were adopted from JAPEX website (https://www.japex.co.jp/english/business/oversea/sadg.html)

It is not a coincidence that our governing relation for the dynamic wetting of capillary tube (equation 5.11) can be reduced to the Washburn equation and directly compared with Darcy's law. All three expressions describe the same phenomenon, but with different assumptions in mind.

In the sections below, we adapt simple situations of flow in capillary tube to qualitatively describe the in-situ oil recovery methods. Equation (5.11) can be then used to justify the recent improvements to the production methods.

5.2 Steam Assisted Gravity Drainage

Steam Assisted Gravity Drainage (SAGD) process has been widely used for in-situ production of bitumen from Athabasca oil sands. The method is normally implemented in deeper sections of the bitumen bearing formation, where open pit mining is not economical. In the SAGD process, two parallel horizontal wells are drilled through the oil sands formation, with one well directly above the other (Figure 5.2a). The steam is injected into the oil sands formation through the top well, which melts the bitumen in oil sands matrix and forms a steam chamber. The melted bitumen phase drains down through the steam chamber walls to the bottom producing well.

The same process can be represented in principle with a flow in a single capillary (Figure 5.2b), with bitumen phase on top and the steam on the bottom. The bitumen flow rate through the capillary is then described by equation (5.11)

$$U = \frac{\sum(P) \, R}{2\zeta + 8\mu L \frac{1}{R(1+4L_m/R)^2}}$$

We can now expand the contributing pressure terms for $\sum(P)$ in the above equation. The bitumen phase is significantly denser than the steam, and thus $\rho g L$ drives the fluid flow to the bottom. At the same time, bitumen tends to spread easily on the sand surface when surrounded with vapour. Therefore, bitumen adhesion to the sand matrix is significant, and $\frac{2\gamma cos\theta}{R}$ resists the flow. The final expression for the bitumen flow in the capillary tube in Figure 5.2b is:

$$U = \frac{(\rho g L - \frac{2\gamma cos\theta}{R}) \, R}{2\zeta + 8\mu L \frac{1}{R(1+4L_m/R)^2}} \tag{5.16}$$

We can see from the above equation that when the hot steam reduces bitumen viscosity, it also reduces the magnitude of both flow rate limiting factors (ζ is directly proportional to μ according to equation 4.1). Therefore, the resistance to flow drops significantly, and bitumen drains under effect of gravity.

Much like the hybrid process described in section 4.2.6, bitumen viscosity can be also reduced with addition of solvents. The viscosity can be then reduced to the same levels as the traditional SAGD process, but it can be done at lower steam temperatures. Moreover, as it has been demonstrated in [19], addition of diluents can reduce the bitumen interface tension significantly. Therefore, the solvent addition also reduces the magnitude of $\frac{2\gamma cos\theta}{R}$, which increases the driving force for the fluid flow in equation (5.16). This process has been implemented in the industry as Expanding Solvent (ES) SAGD process.

The SAGD process can be further improved by simply trying to increase the driving force and reduce the rate-limiting factors in equation (5.16). As an example, the pH of the steam can be brought to 11. The higher pH of the steam would then
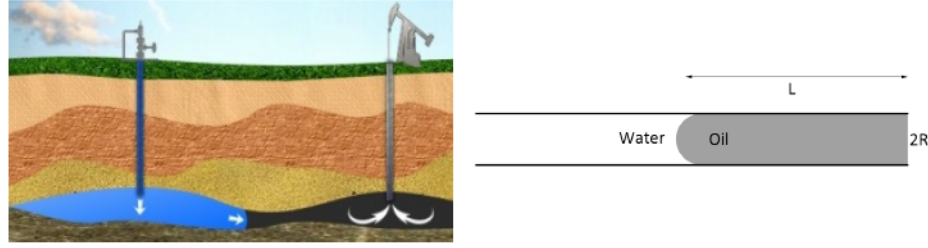
FIGURE 5.3: Schematic representation of water flooding. The image on the right represents a schematic water flooding process in a single capillary tube. The image on the left was adopted from Amerex website (http://www.amerexco.com/recovery.html)

reduce the interfacial tension of bitumen. It would also hydrolyze and deprotonate the sand surface very quickly since high pH is also coupled with high temperature. Overall, equation (5.16) can be used as a guide when introducing chemicals or changing conditions to improve the SAGD process.

5.3   Conventional Oil Recovery: Water Flooding

Water flooding is the most commonly used technique for increasing production rates in conventional oil recovery. The whole reservoir is normally split into production patterns, where some of the wells inject water into the reservoir while the rest of the wells produce oil (Figure 5.3a). The injected water phase displaces oil from the pores and maintains the pressure differential across the reservoir. Thus, the efficiency of the method depends on the oil viscosity and interactions of the water phase with the rock.

The water flooding can be qualitatively represented with the immiscible liquid displacement in a capillary tube (Figure 5.3a). In this case, an external pressure differential ΔP is applied across the tube. We can neglect the gravity effects, while capillary forces either assist the flow or resist it depending on the rock wettability. Therefore, the overall governing relation for displacement rate can be expressed as:

$$U = \frac{\left(-\Delta P \pm \frac{2\gamma cos\theta}{R}\right) R}{2\zeta + 8(\mu_o L_o + \mu_w L_w)\frac{1}{R(1+4L_m/R)^2}} \tag{5.17}$$

By analyzing equation (5.17), we can qualitatively explain some of the common observations in conventional oil recovery.

First of all, water flooding is normally not very effective in oil-wet reservoirs. In this situations, the oil has high affinity to the rock, and thus the wetting line friction coefficient will have significantly large value. Moreover, the capillary forces will resist the flow, and $\frac{2\gamma cos\theta}{R}$ will carry a positive sign.

Secondly, one normally has to apply higher pressure differential ΔP, when the typical size of the pore R is small. Looking at equation (5.17), we can see that the driving force contribution due to applied pressure differential ($R\,\Delta P$) reduces in magnitude for smaller pore sizes. Moreover, the associated hydrodynamic energy losses ($\frac{8(\mu_o L_o + \mu_w L_w)}{R(1+4L_m/R)^2}$) become higher in smaller pores. It is interesting to note that both terms related to the rock-liquid interactions ($\frac{2\gamma cos\theta}{R}R$ and 2ζ) are independent of the geometry.

The liquid-solid interactions take progressively more important role in water-flooding designs. It has been demonstrated that the presence of certain ions in water phase can improve oil recovery by water flooding [43, 44]. The method is often referred to as "Smart Water Flooding". Much like in our droplet recession experiments, the rock wettability can be effectively modified with ion addition. For instance, when the rock is mainly composed of sandstone, its affinity to water can be modified by increasing water pH. It has been demonstrated in section 4.2.2 that the addition of $NaOH$ effectively reduces the wetting line friction coefficient, promoting faster liberation rates.

Chapter 6

Conclusions

Bitumen liberation is an important step in minable oil sands extraction process. At this step, bitumen phase recedes from the sand grain surfaces to form truncated spherical caps. The final shape of these droplets is normally defined by the static contact angle, measured from the water phase. If the final angle is small, bitumen droplets are easily detached from the solid by hydrodynamic shear force of the next step of the extraction process and/or by aeration. It is therefore important that each bitumen droplet reaches its final shape as fast as possible. Hence, understanding major rate-defining parameters is crucial for optimizing bitumen liberation.

6.1 Thesis Contributions

In this study, we conducted a series of experiments in an attempt to mimic bitumen liberation from a single sand grain surface. This was done by fabricating micro-spherical glass tips and coating them with bitumen in air. Each of the "oil sand grains" was then immersed in aqueous solution, where bitumen spontaneously receded from the glass surface.

The bitumen droplet recession was modeled utilizing the theory of wetting dynamics. Three of the major dynamic wetting models were applied to our system.

While it has been demonstrated that the combined molecular-hydrodynamic model is appropriate at capillary numbers above 10^{-2}, molecular-kinetic model was used to analyze slow bitumen recession at room temperature.

We explored the effects of aqueous solution pH, presence of sodium and calcium ions, and solid wettability on the bitumen liberation rates. The resistance to flow (bitumen recession) at the contact line was shown to decrease at smaller values of work of adhesion. Moreover, we confirmed that both diluent addition and increase in temperature can assist in faster bitumen liberation.

All of the experiment results in this study were analyzed in light of wetting dynamics theory. It was found that $\frac{\gamma_{BW}}{\mu_b}$ and the work of adhesion W_a have significant impact on the bitumen liberation rates. Ideally, one would want to increase the parameter $\frac{\gamma_{BW}}{\mu_b}$, while keeping the work of adhesion as low as possible. In such systems the bitumen phase would be displaced quickly, while making the droplets easily detachable from the sand grain surface.

We extended our understanding of wetting dynamics to the wetting in a capillary tube. The model for the flow was developed and compared with the Washburn equation. This model was then used to qualitatively analyze the flow in porous media, with the particular focus to ES SAGD and smart water flooding. It was found that the production rates for these processes are rate-limited by mechanisms similar to the bitumen liberation.

6.2 Future Work

Most of the experiments performed in this study were done at room temperature. However, the current oil sands extraction process runs at about 50°C. Thus, it would be of interest to confirm whether the effects of aqueous solution chemistry and solid wettability also hold at higher temperatures.

Moreover, we demonstrated that the molecular-kinetic model fits the droplet recession data nicely, when the experiment is performed at capillary numbers below 10^{-2}. Above that number we proposed that a combined consideration of molecular-kinetic and hydrodynamic models is needed. However, the molecular-hydrodynamic model used in this thesis is only a combination of simplified molecular-kinetic and hydrodynamic models. As a result, it does not fit experimental data nicely over the full range of small capillary numbers. Therefore, there is still room for an improved model that would take into account both molecular processes at the contact line and viscous resistance to the flow.

The modern dynamic wetting theory is overwhelmingly focused on experiments at capillary numbers below one, where the shape of the interface is mainly controlled by surface or interfacial tension. At the same time, it would be interesting to see if the wetting behaviour would change significantly at capillary numbers close to one. Here, one could expect a more pronounced viscous "foot" at the three phase contact line, which was already observed in a few of our faster droplet recession experiments.

Furthermore, one could test the proposed relationship (section 5.1.1) for wetting in capillary tubes. In particular, this could be done by simply observing the capillary rise of different liquids in a micro-scale capillary tubes. Then it could be tested if the same relationship also holds for rise of the liquid column in porous materials.

Bibliography

[1] *Facts about Albertas oil sands and its industry.* Oil Sands Discovery Centre. URL `http://history.alberta.ca/oilsands/resources/docs/facts_sheets09.pdf`.

[2] J. H. Masliyah, Z. Xu, and J. A. Czarnecki. *Handbook on Theory and Practice of Bitumen Recovery from Athabasca Oil Sands.* Number v. 2 in Handbook on Theory and Practice of Bitumen Recovery from Athabasca Oil Sands. Kingsley Publishing Services, 2011. ISBN 9781926832166. URL `http://books.google.ca/books?id=OLPIMAEACAAJ`.

[3] K. A. Clark and D. S. Pasternack. Hot water seperation of bitumen from alberta bituminous sand. *Industrial and Engineering Chemistry*, 24(12):1410–1416, 1932. doi: 10.1021/ie50276a016. URL `http://pubs.acs.org/doi/abs/10.1021/ie50276a016`.

[4] A. Vrij. Possible mechanism for the spontaneous rupture of thin, free liquid films. *Discuss. Faraday Soc.*, 42:23–33, 1966. doi: 10.1039/DF9664200023. URL `http://dx.doi.org/10.1039/DF9664200023`.

[5] A. Sheludko. Thin liquid films. *Advances in Colloid and Interface Science*, 1(4):391 – 464, 1967. ISSN 0001-8686. doi: http://dx.doi.org/10.1016/0001-8686(67)85001-2. URL `http://www.sciencedirect.com/science/article/pii/0001868667850012`.

[6] E. Ruckenstein and R. K. Jain. Spontaneous rupture of thin liquid films. *J. Chem. Soc., Faraday Trans. 2*, 70:132–147, 1974. doi: 10.1039/F29747000132. URL `http://dx.doi.org/10.1039/F29747000132`.

[7] J. R. Walker. *The Recession of Bitumen from a Silica Surface Under Shear Flow*. Canadian theses. University of Alberta (Canada), 2006. ISBN 9780494224007. URL `http://books.google.ca/books?id=TlmOD2imPvAC`.

[8] S. Basu, K. Nandakumar, and J. H. Masliyah. A study of oil displacement on model surfaces. *Journal of Colloid and Interface Science*, 182(1):82 – 94, 1996. ISSN 0021-9797. doi: http://dx.doi.org/10.1006/jcis.1996.0439. URL `http://www.sciencedirect.com/science/article/pii/S0021979796904397`.

[9] E. B. Dussan. On the spreading of liquids on solid surfaces: Static and dynamic contact lines. *Annual Review of Fluid Mechanics*, 11(1):371–400, 1979. doi: 10.1146/annurev.fl.11.010179.002103. URL `http://dx.doi.org/10.1146/annurev.fl.11.010179.002103`.

[10] P. G. de Gennes. Wetting: statics and dynamics. *Rev. Mod. Phys.*, 57:827–863, Jul 1985. doi: 10.1103/RevModPhys.57.827. URL `http://link.aps.org/doi/10.1103/RevModPhys.57.827`.

[11] T. D. Blake. The physics of moving wetting lines. *Journal of Colloid and Interface Science*, 299(1):1 – 13, 2006. ISSN 0021-9797. doi: http://dx.doi.org/10.1016/j.jcis.2006.03.051. URL `http://www.sciencedirect.com/science/article/pii/S0021979706002463`.

[12] R. T. Foister. The kinetics of displacement wetting in liquid/liquid/-solid systems. *Journal of Colloid and Interface Science*, 136(1):266 – 282, 1990. ISSN 0021-9797. doi: http://dx.doi.org/10.1016/0021-9797(90)90097-8. URL `http://www.sciencedirect.com/science/article/pii/0021979790900978`.

[13] R. G. Cox. The dynamics of the spreading of liquids on a solid surface. part 1. viscous flow. *Journal of Fluid Mechanics*, 168:169–194, 7 1986. ISSN 1469-7645. doi: 10.1017/S0022112086000332. URL `http://journals.cambridge.org/article_S0022112086000332`.

[14] M. Fermigier and P. Jenffer. An experimental investigation of the dynamic contact angle in liquid-liquid systems. *Journal of Colloid and Interface Science*, 146(1):226 – 241, 1991. ISSN 0021-9797. doi: http://dx.doi.org/10.1016/0021-9797(91)90020-9. URL `http://www.sciencedirect.com/science/article/pii/0021979791900209`.

[15] P. Sheng and M. Zhou. Immiscible-fluid displacement: Contact-line dynamics and the velocity-dependent capillary pressure. *Phys. Rev. A*, 45:5694–5708, Apr 1992. doi: 10.1103/PhysRevA.45.5694. URL `http://link.aps.org/doi/10.1103/PhysRevA.45.5694`.

[16] T. D. Blake and J. M. Haynes. Kinetics of liquid-liquid displacement. *Journal of Colloid and Interface Science*, 30(3):421 – 423, 1969. ISSN 0021-9797. doi: http://dx.doi.org/10.1016/0021-9797(69)90411-1. URL `http://www.sciencedirect.com/science/article/pii/0021979769904111`.

[17] M. Ramiasa, J. Ralston, R. Fetzer, and R. Sedev. Contact line friction in liquid-liquid displacement on hydrophobic surfaces. *The Journal of Physical Chemistry C*, 115(50):24975–24986, 2011. doi: 10.1021/jp209140a. URL `http://pubs.acs.org/doi/abs/10.1021/jp209140a`.

[18] R. Fetzer, M. Ramiasa, and J. Ralston. Dynamics of liquid-liquid displacement. *Langmuir*, 25(14):8069–8074, 2009. doi: 10.1021/la900584s. URL `http://pubs.acs.org/doi/abs/10.1021/la900584s`. PMID: 19496572.

[19] F. Lin, L. He, B. Primkulov, and Z. Xu. Dewetting dynamics of a solid microsphere by emulsion drops. *The Journal of Physical Chemistry C*, 118 (25):13552–13562, 2014. doi: 10.1021/jp412662x. URL `http://pubs.acs.org/doi/abs/10.1021/jp412662x`.

[20] A. Yeung, T. Dabros, J. Masliyah, and J. Czarnecki. Micropipette: a new technique in emulsion research. *Colloids and Surfaces A: Physicochemical and Engineering Aspects*, 174(12):169 – 181, 2000. ISSN 0927-7757. doi: http://dx.doi.org/10.1016/S0927-7757(00)00509-4. URL `http://www.sciencedirect.com/science/article/pii/S0927775700005094`.

[21] A. Yeung, K. Moran, J. Masliyah, and J. Czarnecki. Shear-induced coalescence of emulsified oil drops. *Journal of Colloid and Interface Science*, 265(2):439 – 443, 2003. ISSN 0021-9797. doi: http://dx.doi.org/10.1016/S0021-9797(03)00531-9. URL `http://www.sciencedirect.com/science/article/pii/S0021979703005319`.

[22] A. Yeung, T. Dabros, J. Czarnecki, and J. Masliyah. On the interfacial properties of micrometre-sized water droplets in crude oil. *Proceedings: Mathematical, Physical and Engineering Sciences*, 455(1990):pp. 3709–3723, 1999. ISSN 13645021. URL `http://www.jstor.org/stable/53505`.

[23] A. Yeung, T. Dabros, and J. Masliyah. Does equilibrium interfacial tension depend on method of measurement? *Journal of Colloid and Interface Science*, 208(1):241 – 247, 1998. ISSN 0021-9797. doi: http://dx.doi.org/10.1006/jcis.1998.5807. URL `http://www.sciencedirect.com/science/article/pii/S0021979798958076`.

[24] O. P. Strausz and E. M. Lown. *The Chemistry of Alberta Oil Sands, Bitumens and Heavy Oils*. Alberta Energy Research Institute, 2003. ISBN 9780778530961. URL `http://books.google.ca/books?id=kKRaAAAACAAJ`.

[25] K. Moran, A. Yeung, and J. Masliyah. Shape relaxation of an elongated viscous drop. *Journal of Colloid and Interface Science*, 267(2): 483 – 493, 2003. ISSN 0021-9797. doi: http://dx.doi.org/10.1016/j.jcis.2003.07.014. URL `http://www.sciencedirect.com/science/article/pii/S0021979703007781`.

[26] C. Huh and L. E. Scriven. Hydrodynamic model of steady movement of a solid/liquid/fluid contact line. *Journal of Colloid and Interface Science*, 35(1):85 – 101, 1971. ISSN 0021-9797. doi: http://dx.doi.org/10.1016/0021-9797(71)90188-3. URL `http://www.sciencedirect.com/science/article/pii/0021979771901883`.

[27] R. G. Cox. The dynamics of the spreading of liquids on a solid surface. part 2. surfactants. *Journal of Fluid Mechanics*, 168:195–220, 7 1986. ISSN 1469-7645. doi: 10.1017/S0022112086000344. URL `http://journals.cambridge.org/article_S0022112086000344`.

[28] O. V. Voinov. Hydrodynamics of wetting. *Fluid Dynamics*, 11(5):714–721, 1976. ISSN 0015-4628. doi: 10.1007/BF01012963. URL `http://dx.doi.org/10.1007/BF01012963`.

[29] S. Glasstone, K. J. Laidler, and H. Eyring. *The Theory of Rate Processes: The Kinetics of Chemical Reactions, Viscosity, Diffusion and Electrochemical Phenomena*. International chemical series. McGraw-Hill Book Company, Incorporated, 1941. URL `http://books.google.ca/books?id=zb2GAAAAIAAJ`.

[30] M. J. de Ruijter, J. De Coninck, and G. Oshanin. Droplet spreading: Partial wetting regime revisited. *Langmuir*, 15(6):2209–2216, 1999. doi: 10.1021/la971301y. URL `http://pubs.acs.org/doi/abs/10.1021/la971301y`.

[31] T. D. Blake and J. De Coninck. The influence of solid-liquid interactions on dynamic wetting. *Advances in Colloid and Interface Science*, 96 (1–3):21 – 36, 2002. ISSN 0001-8686. doi: http://dx.doi.org/10.1016/S0001-8686(01)00073-2. URL `http://www.sciencedirect.com/science/article/pii/S0001868601000732`. A Collection of Papers in Honour of Nikolay Churaev on the Occasion of his 80th Birthday.

[32] K. Moran and A. Yeung. Determining bitumen viscosity through drop shape recovery. *The Canadian Journal of Chemical Engineering*, 82(4):813–820, 2004. ISSN 1939-019X. doi: 10.1002/cjce.5450820421. URL `http://dx.doi.org/10.1002/cjce.5450820421`.

[33] J. Ralston and G. Newcombe. *Static and Dynamic Contact Angles*. Developments in mineral processing. Elsevier, 1992. URL `http://books.google.ca/books?id=MQhAnQEACAAJ`.

[34] G. Hanly, D. Fornasiero, J. Ralston, and R. Sedev. Electrostatics and metal oxide wettability. *The Journal of Physical Chemistry C*, 115(30):14914–14921,

2011. doi: 10.1021/jp203714a. URL http://pubs.acs.org/doi/abs/10.1021/jp203714a.

[35] J. Liu, Z. Xu, and J. Masliyah. Studies on bitumen-silica interaction in aqueous solutions by atomic force microscopy. *Langmuir*, 19(9):3911–3920, 2003. doi: 10.1021/la0268092. URL http://pubs.acs.org/doi/abs/10.1021/la0268092.

[36] K. Takamura and D. Wallace. The physical chemistry of the hot water process. *Journal of Canadian Petroleum Technology*, 27(6):98–106, 1988. ISSN 0021-9487. doi: 10.2118/88-06-08. URL http://dx.doi.org/10.2118/88-06-08.

[37] S. Basu, K. Nandakumar, and J. H. Masliyah. Effect of nacl and mibc/kerosene on bitumen displacement by water on a glass surface. *Colloids and Surfaces A: Physicochemical and Engineering Aspects*, 136(12):71 – 80, 1998. ISSN 0927-7757. doi: http://dx.doi.org/10.1016/S0927-7757(97)00251-3. URL http://www.sciencedirect.com/science/article/pii/S0927775797002513.

[38] S. K. Harjai, C. Flury, J. Masliyah, J. Drelich, and Z. Xu. Robust aqueous-nonaqueous hybrid process for bitumen extraction from mineable athabasca oil sands. *Energy and Fuels*, 26(5):2920–2927, 2012. doi: 10.1021/ef300270j. URL http://pubs.acs.org/doi/abs/10.1021/ef300270j.

[39] L. He, F. Lin, X. Li, Z. Xu, and H. Sui. Enhancing bitumen liberation by controlling interfacial tension and viscosity ratio through solvent addition. *Energy and Fuels*, 0(ja):null, 0. doi: 10.1021/ef501963e. URL http://dx.doi.org/10.1021/ef501963e.

[40] W. M. Deen. *Analysis of Transport Phenomena*. Topics in Chemical Engineering. OUP USA, 2012. ISBN 9780199740253. URL http://books.google.ca/books?id=eJlFpwAACAAJ.

[41] E. W. Washburn. The dynamics of capillary flow. *Phys. Rev.*, 17:273–283, Mar 1921. doi: 10.1103/PhysRev.17.273. URL http://link.aps.org/doi/10.1103/PhysRev.17.273.

[42] L. R. Fisher and P. D. Lark. An experimental study of the washburn equation for liquid flow in very fine capillaries. *Journal of Colloid and Interface Science*, 69(3):486 – 492, 1979. ISSN 0021-9797. doi: http://dx.doi.org/10.1016/0021-9797(79)90138-3. URL `http://www.sciencedirect.com/science/article/pii/0021979779901383`.

[43] A. M. Al-sofi and A. A. Yousef. Insight into smart-water recovery mechanism through detailed history matching of coreflood experiments. *Society of Petroleum Engineers*, 2013. ISSN 978-1-61399-268-5. doi: http://dx.doi.org/10.2118/166035-MS.

[44] A. A. Yousef, J. S. Liu, G. W. Blanchard, S. Al-Saleh, T. Al-Zahrani, R. M. Al-zahrani, H. I. Tammar, and N. Al-mulhim. Smart waterflooding: Industry. *Society of Petroleum Engineers*, 2012. ISSN 978-1-61399-213-5. doi: http://dx.doi.org/10.2118/159526-MS.

[45] R. L. Hoffman. A study of the advancing interface. i. interface shape in liquid-gas systems. *Journal of Colloid and Interface Science*, 50(2):228 – 241, 1975. ISSN 0021-9797. doi: http://dx.doi.org/10.1016/0021-9797(75)90225-8. URL `http://www.sciencedirect.com/science/article/pii/0021979775902258`.

Appendix A

Automated Angle Acquisition

A.1   Discussion on Apparent Contact Angle

Before we analyze bitumen droplet relaxation images (Figure A.2a), we need to be clear on our definition of apparent contact angle. The curvature of a droplet interface is known to change as it nears contact line, and interface can be separated into *inner* and *outer* regions (Figure A.1). Normally authors only report *macroscopic* contact angles, and very often microscopic distortions of the interface are not visible [30, 45]. In our experiment, the droplet shape in the *outer* region is governed by capillary forces, while interface in the *inner* region is distorted by solid/liquid interactions and dynamic effects. We are particularly interested in *macroscopic* angle evolution and thus adopt a definition similar to one given by Cox [13].

Definition A.1. Apparent contact angle is the angle between bitumen/water interface and solid surface as one approaches contact line in the *outer* region
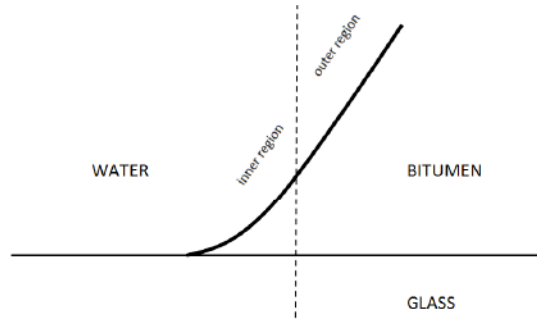
FIGURE A.1: Schematic representation of droplet interface close to contact line

A.2   Motivation for Automated Approach

One way to measure this contact angle would be: printing out the images, drawing tangent lines close to three phase contact line, and estimating contact angles with a protractor. Similar approach was in fact adopted by several investigators [8, 45], and obtaining accurate contact angle readings required careful manual measurements. A slightly improved procedure was possible for our geometry, and was utilized by Lin et al. [19]. ImagePro software was used to fit two circular objects as in Figure A.2e. Once equations of circles were defined, one could easily find circle intersections, corresponding tangent lines and contact angles. However, this process would still be time consuming if one wants to analyze a 600 frame video file. Moreover, the process of fitting the circles in the ImagePro software would still require user judgement, which suggests that different investigators could have different biases in their contact angle readings. Thus, it was decided to implement a more systematic automated approach to contact angle measurement.

A.3   Implementation Steps

Full implementation of automated angle measurement is given at the end of this section as a series of Matlab functions. However, we can describe the key steps involved in the algorithm here.

- First, the input image is converted to black-and-white, and boundary of the resulting object is recorded (Figures A.2a, A.2b, A.2c).

(A) Input image   (B) B/W image   (C) Object boundaries

(D) Detection of edges   (E) Fitting circles   (F) Calculating contact angle
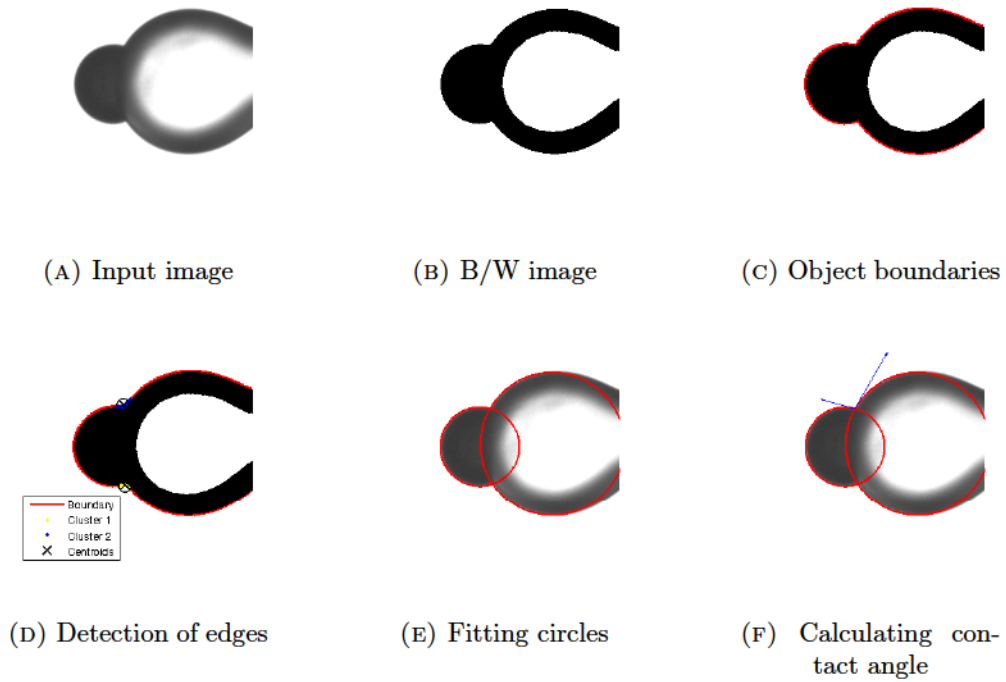
FIGURE A.2: Visual demonstration of key image processing steps

- Then, one needs to separate obtained boundary into bitumen/water and glass/water interfaces in order to fit a circle into each. This is done by noting that contact line points correspond to locations with sharpest change in direction along the boundary. An average deviation angle is computed by constructing several vectors starting at the point of consideration and ending at the neighbouring boundary points (Figure A.3). Angles between red and blue vectors are calculated from dot products, and an average is obtained for the whole neighbourhood. Points with sharper angle deviations produce smaller average angles. Thus, we are able to locate a number of points close to the contact line (Figure A.2d).

Remark A.2. This step is made even more accurate by noting that vector pairs at the contact line will produce cross product pointing outwards (from the paper), while any other points on bitumen/water or glass/water interfaces will have cross products pointing inwards (into the paper). Hence, we significantly improve contact line point detection if we only consider vector pairs with desired cross product orientation in calculating average angle of

the neighbourhood.

- Finally, we can separate the object boundary into bitumen/water and glass/water interfaces. Circles are fitted to each interface in a least square error fashion (Figure A.2e). Intersections of the circles and corresponding tangent lines are calculated. The contact angle values are calculated from the dot products of outwards facing tangent vectors (Figure A.2f).

- Above steps are repeated (looped) for all frames of experimental video file.
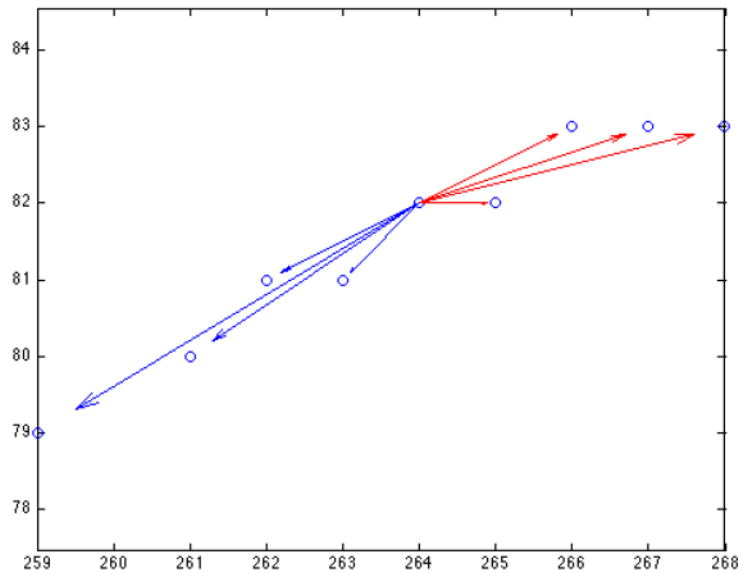
FIGURE A.3: Blue circles are the locations of the boundary points. Red and blue vectors, that start at the point of consideration, are used to calculate average angle deviation at current boundary point location. Axis of the plot are scaled in pixels.

A.4 Comparison to Semi-Manual Measurements from Image-Pro Software

A small study was conducted to compare performance of our automated approach to semi-manual angle measurements with ImagePro. A number of fellow graduate students were asked to perform five contact angle measurements on the same image

(Table A.1). Students used a protractor tool to give their best estimates of the contact angle. As it was anticipated, different people have different biases in their measurements, which further supports the need for an automated approach. The MATLAB implementation of the program was run on the sample experimental video file, and it's relative performance semi-manual measurements are presented in Figure A.4.

TABLE A.1: Results of semi-manual angle measurements

Student	Contact Angle (deg)					Average Angle (deg)
A	68.8	80.1	67.2	69.8	72.4	**71.7**
B	80.2	74.2	79.1	74.7	76.3	**76.9**
C	59.6	61.8	68.1	66.8	61.4	**63.5**
D	72.3	66.2	60.5	64.8	58.1	**64.4**
E	68.7	79.5	61.2	54.5	74.4	**67.6**
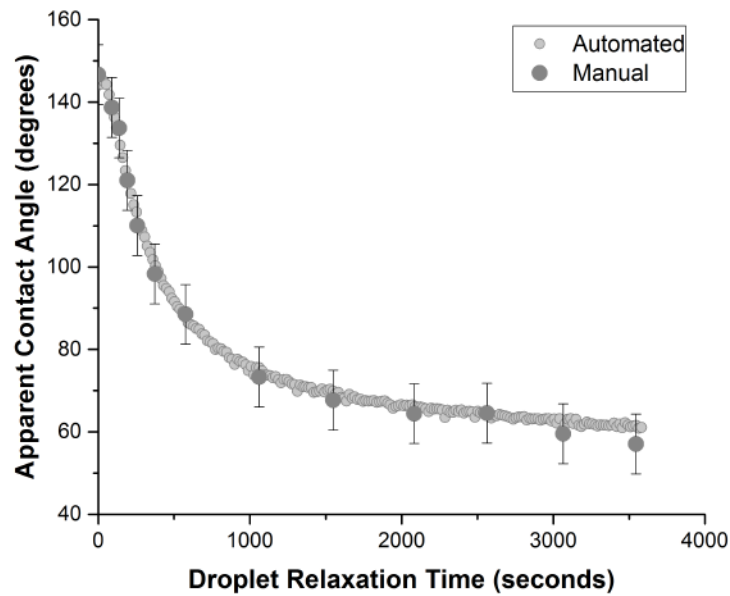
FIGURE A.4: Relative performance of ImagePro measurements and Matlab implementation of automated angle measurements. The error for manual measurements was estimated as a standard deviation of data in Table A.1

A.5 Matlab Source Code

```matlab
function [data,re,rm] = main(file_name,dt)
% This program analyses bitumen micro-droplet recession experiments. The
% program reads in experimental video file (see Primkulov 2014 MSc Thesis)
% and outputs contact line evolution data with time.
%   INPUTS:
%   file_name - name of the video file
%   dt - time interval between video frames (s)
%
%   OUTPUTS:
%   data - matrix that is arranged as follows. 1st column is the time in
%   seconds. 2nd column is the apparent contact angle (Cox 1985).
%   3rd column is size of bitumen-wetted region (Primkulov 2014)

%-------------------------------------------------
% display_option = 1 - display each step
% display_option = 0 - do not display
display_option=1;

% Find number of frames in the video file. trafficObj is later used
% to obtain a single video frame
[nframes,trafficObj]=read_number_of_frames(file_name);

for k=1:nframes
    % Read single image
    singleFrame = read(trafficObj, k);

    % Obtain object boundary
    [boundary] = obtain_boundary(singleFrame);

    [k1,k2]=find_three_phase_contact(boundary);

    % Obtain bitumen/water and glass/water interfaces
    dn=round(0.05*size(boundary,1)); % 5% of the total boundary length
    bitumen=boundary(k1+dn:k2-dn,:);
    glass=vertcat(boundary(k1-3*dn:k1,:),boundary(k2:k2+3*dn,:));

    % Fit circles to bitumen/water and glass/water interfaces
    [radius1,center1]=circfit(bitumen);
    [radius2,center2]=circfit(glass);

    if display_option==1
        figure(1)
        clf
        imshow(singleFrame)
        axis equal;
        hold on
        xlabel('Y-axis')
        ylabel('X-axis')
        title( sprintf( '%s: %d', 'Frame number ', k ) );
        plot_circle(radius1,center1)
        plot_circle(radius2,center2)
    end
```

```matlab
        [angle,l] = angle_circle_circle(center1(1),center1(2),radius1,...
                                center2(1),center2(2),radius2);

        data(k,1)=(k-1)*dt;
        data(k,2)=angle;
        data(k,3)=l;
    end

    [re,rm]=find_re_rm(center1,radius1,center2,radius2);

    figure(2)
    clf
    plot(data(:,1),data(:,2),'bo')
    xlabel('Time(seconds)')
    ylabel('Contact Angle')
    end

    function [nframes,trafficObj] = read_number_of_frames(file_name)
    % This program find the number of frames in the video file.
    trafficObj = VideoReader(file_name);
    nframes = get(trafficObj, 'NumberOfFrames');
    end

    function [boundary] = obtain_boundary(singleFrame)
    % This function obtains object boundary (glass+bitumen)
    % from single frame image


    %-------------------------------------------------
    % display_option = 1 - display each step
    % display_option = 0 - do not display
    display_option=0;

    if display_option==1
        figure(11)
        clf
        imshow(singleFrame)
        axis equal; axis off;
    end

    % Threshold the Image and Convert to B/W
    I = rgb2gray(singleFrame);
    threshold = graythresh(I);
    bw =1-im2bw(I,threshold);

    if display_option==1
        clf
        imshow(bw)
    end

    % remove all object containing fewer than 3000 pixels
    bw = bwareaopen(bw,3000);

    if display_option==1
        clf
        imshow(bw)
    end
```

```matlab
% fill a gap in the pen's cap
se = strel('disk',2);
bw = imclose(bw,se);

% fill any holes, so that regionprops can be used to estimate
% the area enclosed by each of the boundaries
bw = imfill(bw,'holes');
bw=1-bw;

if display_option==1
    clf
    imshow(bw)
end

% Find boundaries
[B,~] = bwboundaries(bw,'noholes');
boundary = B{1};

% Clean boundaries
[rows,~,~] = find(boundary==1);boundary(rows,:)=[];
[rows,~,~] = find(boundary==size(bw,1));boundary(rows,:)=[];
[rows,~,~] = find(boundary==size(bw,2));boundary(rows,:)=[];

if display_option==1
    hold on
    plot(boundary(:,2), boundary(:,1),'r', 'LineWidth', 2)
    hold off
end
end

function [k1,k2]=find_three_phase_contact(boundary)
% This program finds three phase contact line points.
% It does so by finding the points along the border with highest
% angle deviations.

%------------------------------------------------
% display_option = 1 - display each step
% display_option = 0 - do not display
display_option=0;

% Region length that is to be checked at a time on the boundary
dn=round(0.05*size(boundary,1)); % 5% of the total boundary length
angle_data=zeros(size(boundary,1),4);angle_data(:,1)=1:size(boundary,1);
angle_data(:,3)=boundary(:,1);angle_data(:,4)=boundary(:,2);
for k=1+dn:size(boundary,1)-dn

    % Plot sub-region of interest
    if display_option==1
        figure(21)
        clf
        plot(boundary(k-dn:k+dn,2),boundary(k-dn:k+dn,1),'bo')
        axis equal
    end

    % Calculate average slope change angle
    angle=0;
    for i=1:dn
```

```matlab
        v1=[boundary(k-i,1)-boundary(k,1);boundary(k-i,2)-boundary(k,2);0];
        v2=[boundary(k+i,1)-boundary(k,1);boundary(k+i,2)-boundary(k,2);0];
        if display_option==1
            hold on
            quiver(boundary(k,2),boundary(k,1),v1(2),v1(1),'r');
            quiver(boundary(k,2),boundary(k,1),v2(2),v2(1),'b');
            hold off
        end
        if dot([0;0;1],cross(v1,v2))<0
            angle=angle+real(acosd((v1(1)*v2(1)+v1(2)*v2(2))...
                /sqrt(v1(1)^2+v1(2)^2)/sqrt(v2(1)^2+v2(2)^2)));
        end
    end
    angle=angle/dn;angle=180-angle;
    angle_data(k,2)=angle;
end

angle_data=sortrows(angle_data,-2);angle_data_analyze=angle_data(1:dn,:);

[k1,k2]=cluster_coords(angle_data_analyze);
end

function [k1,k2]=cluster_coords(Xinput)
% This function separates input data into two separate clusters
% by location.

%------------------------------------------------
% display_option = 1 - display each step
% display_option = 0 - do not display
display_option=0;


X=Xinput(:,3:4);

% Cluster data into 2 categories
opts = statset('Display','off');
[idx,ctrs,~] = kmeans(X,2,...
                    'Distance','sqEuclidean',...
                    'Replicates',5,...
                    'Options',opts);
if display_option==1
    figure(11)
    hold on
    plot(X(idx==1,2),X(idx==1,1),'y.','MarkerSize',12)
    plot(X(idx==2,2),X(idx==2,1),'b.','MarkerSize',12)
    plot(ctrs(:,2),ctrs(:,1),'kx',...
        'MarkerSize',12,'LineWidth',2)
    plot(ctrs(:,2),ctrs(:,1),'ko',...
        'MarkerSize',12,'LineWidth',2)
    legend('Cluster 1','Cluster 2','Centroids',...
            'Location','W')
    hold off
end


% Find k1
Xinput(:,5)=(Xinput(:,3)-ctrs(1,1)).^2+(Xinput(:,4)-ctrs(1,2)).^2;
Xinput=sortrows(Xinput,5); % puts closest points to top rows
```

```matlab
k1_temp=Xinput(1,1);

% Find k2
Xinput(:,5)=(Xinput(:,3)-ctrs(2,1)).^2+(Xinput(:,4)-ctrs(2,2)).^2;
Xinput=sortrows(Xinput,5); % puts closest points to top rows
k2_temp=Xinput(1,1);

k1=min([k1_temp k2_temp]);
k2=max([k1_temp k2_temp]);
end

function [angle,L0] = angle_circle_circle(xc1,yc1,r1,xc2,yc2,r2)
%------------------------------------------------
% display_option = 1 - display each step
% display_option = 0 - do not display
display_option=0;

    % Calculations
    [xout,yout] = circcirc(xc1,yc1,r1,xc2,yc2,r2);

    xi=xout(1);yi=yout(1);

    % Find tangent vectors
    v1p=[-yi+yc1;xi-xc1];v2p=[yi-yc2;-xi+xc2];
    if display_option==1
        figure(1)
        hold on
        quiver(yi,xi,v1p(2),v1p(1),'b')
        quiver(yi,xi,v2p(2),v2p(1),'b')
        hold off
    end

    ang=pi/2-acos(sqrt((xout(2)-xout(1))^2+(yout(2)-yout(1))^2)/2/r2);
    L0=r2*ang/501*235.6732*10^-6;

    angle=acosd((v1p(1)*v2p(1)+v1p(2)*v2p(2))/sqrt(v1p(1)^2+v1p(2)^2)...
        /sqrt(v2p(1)^2+v2p(2)^2));
end

function plot_circle(radius,center)
ang=0:0.01:2*pi;
xp=radius*cos(ang);
yp=radius*sin(ang);
hold on
plot(center(2)+yp,center(1)+xp,'r','LineWidth',1.5);
hold off
end

function [re,rm] = find_re_rm(center1,radius1,center2,radius2)
%FIND_RE_RM Summary of this function goes here
%   Detailed explanation goes here
[xout,yout] = circcirc(center1(1),center1(2),radius1,...
                                center2(1),center2(2),radius2);
H=radius1+sqrt(radius1^2-(sqrt((xout(1)-xout(end))^2+...
    (yout(1)-yout(end))^2)/2)^2);
h=radius2-sqrt(radius2^2-(sqrt((xout(1)-xout(end))^2+...
    (yout(1)-yout(end))^2)/2)^2);
```

71

```
Vcap=1/3*pi*H^2*(3*radius1-H)-1/3*pi*h^2*(3*radius2-h);
re=((3*Vcap/4/pi)^(1/3))/501*235.6732*10^-6;
rm=radius2/501*235.6732*10^-6;
end
```